Clarke Modet

Carrera 11 No. 86-53, Piso 3
Edificio Segovia
110221 Bogotá, **Colombia**
T (+57) 1 618 10 88
F (+57) 1 635 08 24

P-14468

SUPERINTENDENCIA DE INDUSTRIA Y COMERCIO
DIRECCIÓN DE NUEVAS CREACIONES
E. S. D.

Re: Expediente No. **NC2017/0011437**
Solicitud de patente a nombre de **UTI LIMITED PARTNERSHIP**

Yo, CAROLINA DAZA MONTALVO identificada como aparece al pie de mi firma, domiciliada en la Carrera 11 No. 86-53, obrando como apoderada de la sociedad UTI LIMITED PARTNERSHIP, domiciliada en Alberta, Canadá, solicitante de la patente de la referencia, en respuesta al oficio No. **5527** notificado electrónicamente el 02 de julio de 2019, relacionado con los requerimientos de fondo de la solicitud, y para el cual solicité oportunamente prórroga el 18 de septiembre de 2019, atentamente me permito presentar la siguiente información:

1. Excepción de Patentabilidad

El examinador ha indicado que el objeto de la antigua reivindicación 19 no es patentable de acuerdo con la legislación local. En respuesta a ello, se informa que dicha reivindicación no se incluye en el nuevo capítulo reivindicatorio.

2. Modificación a las Reivindicaciones

Con fundamento en la facultad que confiere el artículo 34 de la Decisión 486 al solicitante para modificar la solicitud de patente en cualquier momento del trámite, presento junto con este memorial nuevo capítulo reivindicatorio, el cual consta de veinticuatro (24) reivindicaciones y reemplaza completamente el presentado anteriormente. Específicamente, se realizaron las siguientes modificaciones:

2.1 No se incluye la antigua reivindicación 19.

2.2 Se eliminaron las expresiones "*o un fragmento de la misma*" de las antiguas

Carrera 11 No. 86-53, Piso 3
Edificio Segovia
110221 Bogotá, **Colombia**
T (+57) 1 618 10 88
F (+57) 1 635 08 24

reivindicaciones 2, 3, 10, 11, y "*o un fragmento o un equivalente de cada uno de ellos*" de las antiguas reivindicaciones 7 y 16.

2.3 Se modificaron las antiguas reivindicaciones 4 y 12 a fin de recitar "*[e]l complejo de una cualquiera de las reivindicaciones (…), en el que el complejo comprende además una capa externa biocompatible, en el que dicha capa biocompatible comprende poli(etilenglicol)*".

2.4 Se eliminó el término "*relevante*" de los ítems a) y k) de la antigua reivindicación 7, así como de las antiguas reivindicaciones 9, 17, 18 y 20.

2.5 Las reivindicaciones y sus dependencias han sido reenumeradas, en vista de las modificaciones mencionadas.

En cuanto a estas modificaciones, me permito decir que las mismas no amplían de ninguna manera la materia objeto de la presente solicitud y se realizaron con el ánimo de superar las objeciones de claridad, unidad de invención y nivel inventivo planteadas por el examinador en su concepto técnico.

3. Pago de tasas

En relación con el número de reivindicaciones, atentamente nos permitimos decir que no se adjunta tasa por concepto de reivindicaciones adicionales, toda vez que el nuevo capítulo reivindicatorio tiene un menor número de reivindicaciones que el anteriormente presentado, y en esencia es el mismo objeto, pero definido con mayor claridad.

4. Claridad y concisión de las reivindicaciones

El solicitante manifiesta que mediante la presentación del nuevo capítulo reivindicatorio quedan subsanadas la totalidad de las objeciones, de modo tal que las nuevas reivindicaciones proporcionan claridad y concisión a la invención descrita, siguiendo las recomendaciones realizadas por el examinador en su concepto técnico.

4.1 Su Despacho ha indicado que las antiguas reivindicaciones 1 a 3, 7, 9 a 11 y 21 a 25 no son concisas porque hacen referencia a múltiples posibilidades, lo cual genera una cantidad indeterminada de posibles elementos antigénicos de MHC-II asociados a nanopartículas metálicas presentando una excesiva complejidad, y dificultando la determinación del verdadero alcance que se busca proteger. En

Carrera 11 No. 86-53, Piso 3
Edificio Segovia
110221 Bogotá, **Colombia**
T (+57) 1 618 10 88
F (+57) 1 635 08 24

dicho respecto, el solicitante respetuosamente manifiesta que considerando los argumentos que serán presentados más adelante en relación con el nivel inventivo de la invención, la objeción realizada por el examinador es incorrecta ya que el alcance de las reivindicaciones se dirige hacia los complejos de nanopartículas que comprenden un conector maleimida- polietilenglicol (PEG). Además, la eficacia terapéutica de las nanopartículas reivindicadas está conectada por un único mecanismo funcional que es generalizable a un antígeno conocido, que puede determinar el experto en la materia. Por ejemplo, véase el documento "*Peptide-MHC-based nanomedicines for autoimmunity function as T-cell receptor microclustering devices*", *Nature Nanotechnology*, 2017 julio; 12 (7): 701-710 (denominado en el presente documento "*Publicación*" y presentado en el Apéndice adjunto) en la página 707, "*Por lo tanto, la densidad de pMHC controla la conversión de Treg al promover el ensamblaje sostenido de los microclusters de TCR, lo que lleva a una señalización de TCR rápida, robusta y prolongada*". Por lo tanto, la eficacia de la conversión de células Treg se ve facilitada por los aspectos estructurales del conector de maleimida que permite para una valencia, direccionalidad y solubilidad adecuadas.

4.2 En relación con la objeción a las antiguas reivindicaciones 4 y 12, tal como se indicó previamente, dichas reivindicaciones fueron modificadas con el propósito de indicar que la capa biocompatible "*comprende poli(etilenglicol*)".

4.3 Adicionalmente, tal como se indicó previamente, la antigua reivindicación 21 fue modificada con el propósito de eliminar el término "*relevante*", lo que limita aún más el alcance de la reivindicación. Además, el solicitante manifiesta que el experto en la técnica basado en las reivindicaciones y los péptidos reivindicados, no tendría dificultades para determinar el alcance de las reivindicaciones. Por tanto, el solicitante respetuosamente solicita que la objeción en cuestión sea retirada.

En consecuencia, nos permitimos indicar que el presente capítulo reivindicatorio, que incluye veinticuatro (24) reivindicaciones, se ajusta a las disposiciones del artículo 30 de la Decisión 486/00.

5. Unidad de Invención

Su Despacho ha indicado que "*[l]a solicitud carece de unidad de invención, debido a que reclama más de un grupo inventivo sin la presencia de características o elementos*

Carrera 11 No. 86-53, Piso 3
Edificio Segovia
110221 Bogotá, **Colombia**
T (+57) 1 618 10 88
F (+57) 1 635 08 24

técnicos nuevos e inventivos que son comunes a todas las invenciones". En dicho respecto, teniendo en cuenta los argumentos que serán presentados más adelante en relación con el nivel inventivo de la invención, el solicitante respetuosamente afirma que las reivindicaciones reclamadas poseen unidad de invención debido a la inclusión del enlazador maleimida-PEG. De esta forma, la objeción al respecto ha sido superada.

No obstante lo anterior, el solicitante se reserva el derecho de presentar solicitudes divisionales dirigidas a la materia que no ha sido incluida en esta oportunidad.

6. Nivel Inventivo

El examinador establece en su concepto técnico la falta de nivel inventivo de las antiguas reivindicaciones 1 a 18, 20 y 21 en vista de las divulgaciones de los documentos WO2008/109852 (D1) y WO2014/080286 (D2).

En este sentido, me permito señalar que el artículo 18 de la Decisión 486 establece que "*Se considerará que una invención tiene nivel inventivo, si para una persona del oficio normalmente versada en la materia técnica correspondiente, esa invención no hubiese resultado obvia ni se hubiese derivado de manera evidente del estado de la técnica*".

Lo anterior significa que el análisis de nivel inventivo **NO** es una comparación de los objetos de las anterioridades y la solicitud en estudio. El análisis de nivel inventivo **debe demostrar** la obviedad de la invención y establecer cómo ésta no contiene un salto cualitativo, que demuestre su altura inventiva, teniendo en cuenta que se hace **necesario demostrar** que la invención analizada carece de nivel inventivo y hubiese sido obvia para una persona versada en la materia.

Considerando la anterior definición y teniendo en cuenta las modificaciones realizadas a las reivindicaciones, es deseo del solicitante manifestar que la invención reclamada en el nuevo capítulo reivindicatorio es inventiva en relación con el estado de la técnica citado, por las siguientes razones:

El examinador afirma que el problema técnico objetivo que las reivindicaciones buscan resolver es "*cómo modificar el complejo de nanopartículas divulgado en el documento D2, para obtener complejos de nanopartícula alternativos que comprendan antígenos MHC tipo II*". Además, el examinador alega que la diferencia entre la invención reclamada y las enseñanzas de D2 consiste en las diferencias dentro del núcleo metálico y que "*no se evidencia un efecto técnico asociado a esta diferencia*" (página 7 del oficio

Clarke Modet

Carrera 11 No. 86-53, Piso 3
Edificio Segovia
110221 Bogotá, **Colombia**
T (+57) 1 618 10 88
F (+57) 1 635 08 24

que se contesta). Ante ello, el solicitante respetuosamente manifiesta su desacuerdo con ambas afirmaciones.

El solicitante afirma que el problema técnico abordado por las reivindicaciones es: cómo proporcionar de manera efectiva y eficiente complejos terapéuticos de nanopartículas que comprendan complejos de nanopartículas de MHC (pMHC-NPC) con densidades específicas de pMHC terapéuticamente relevantes. Al abordar este problema, el solicitante ha descubierto que los enlazadores funcionalizados con PEG que acoplan el pMHC al núcleo de nanopartículas de particular interés terapéutico poseen las siguientes características: (1) los enlazadores permiten una valencia y densidad umbral con respecto al acoplamiento de pMHC, (2) los enlazadores disponibles para unir el pMHC a la nanopartícula logran una orientación particular con respecto a las nanopartículas, y (3) los enlazadores no deberían agregarse y deberían promover la solubilidad y la estabilidad de los NPC. La presente invención reivindicada posee estas características (1), (2) y (3), y aborda los problemas que presentan los complejos que **no** poseen estas características en la síntesis de pMHC-NPC terapéuticos. El solicitante ha descubierto que los pMHC-NPC que comprenden un conector PEG funcionalizado con maleimida, como se reivindica actualmente, abordan estos problemas.

En apoyo de las afirmaciones anteriores, el solicitante presenta para la referencia adicional del examinador un artículo de investigación publicado por el inventor titulado "*Las nanomedicinas basadas en péptidos-MHC para la función de autoinmunidad como dispositivos de microclustering de receptores de células T*" ("*Peptide-MHC-based nanomedicines for autoimmunity function as T-cell receptor microclustering devices*", *Nature Nanotechnology*, 2017 julio; 12 (7): 701-710 – denominado en el presente documento "*Publicación*" y presentado en el Apéndice adjunto), en donde las propiedades superiores del enlazador maleimida-PEG reivindicado con respecto a la valencia, direccionalidad y solubilidad se demuestran aún más.

Como se establece en la Publicación y la presente solicitud, la valencia y densidad de pMHC son factores clave en las propiedades terapéuticas de los pMHC-NPC. Los pMHC-NPC reivindicados actualmente, que comprenden un conector maleimida-PEG, permiten una conjugación de pMHC altamente densa y altamente valente. La presente solicitud, así como la Publicación, demuestran los efectos terapéuticos de la valencia y la densidad utilizando los enlazadores maleimida-PEG (véase, por ejemplo, el párrafo [0402], el Ejemplo 3 en párrafos [0474] - [0476] y la Figura 22A-B de la solicitud PCT). La Publicación respalda aún más la presente solicitud al demostrar que los enlazadores maleimida-PEG superan un umbral de valencia y densidad (ver la Publicación, Tabla

Carrera 11 No. 86-53, Piso 3
Edificio Segovia
110221 Bogotá, **Colombia**
T (+57) 1 618 10 88
F (+57) 1 635 08 24

complementaria 2, fila que contiene "*Óxido de hierro PF-M*") para mejorar la formación de células T reguladoras (Treg) y/o expansión (ver la Publicación, páginas 702-703, y las Figuras 2-3 en páginas 703-704).

La direccionalidad u orientación no aleatoria del extremo funcionalizado del conector de PEG también es un factor deseado de la eficacia terapéutica. La utilización del conector de maleimida-PEG reivindicado da como resultado una visualización direccional del extremo funcionalizado con maleimida de la molécula de PEG disponible para la conjugación de pMHC. El conector maleimida-PEG permite la conjugación direccional de pMHC a través de la cisteína carboxiterminal (véase el párrafo [0413] y la Tabla 1 de la presente solicitud). Los datos experimentales publicados respaldan aún más dicha divulgación (véase la Publicación, Figura 1 y la Tabla complementaria 2, fila que contiene "*Óxido de hierro PF-M*"). En particular, el enlazador maleimida-PEG proporciona resultados superiores con respecto a la direccionalidad en comparación con otros enlazadores (véase la Publicación, Tabla complementaria 2).

La solubilidad y la no agregación es otra característica terapéuticamente relevante para los pMHC-NPC. El conector de maleimida-PEG reivindicado produce pMHC-NPC solubles que pueden usarse para lograr un efecto terapéutico. La Publicación demuestra además que la utilización del conector maleimida-PEG da como resultado pMHC-NPC solubles (véase los párrafos [0412], [0415], y los Ejemplos 1-3 de la presente solicitud; así como también la Publicación en página 702 y la Tabla complementaria 2 , fila que contiene "*Óxido de hierro PF-M*").

El solicitante afirma respetuosamente que la invención reivindicada en esta solicitud proporciona una solución técnica que proporciona valencia, direccionalidad y solubilidad terapéuticamente deseables. Un experto en la materia y con el problema técnico no habría llegado a los complejos de nanopartículas actualmente reivindicados confiando en cualquier combinación de D1 y/o D2, al menos por la razón de que las propiedades beneficiosas de los enlazadores maleimida-PEG no se revelan en la técnica anterior. Como tal, los solicitantes han descubierto una solución inventiva y novedosa, en los complejos de nanopartículas reivindicados que comprenden un conector maleimida-PEG, a problemas de actividad agonista de la activación de células TR1 por nanopartículas de pMHC. Por lo tanto, el solicitante respetuosamente solicita que las objeciones realizadas sean retiradas.

De esta forma, las nuevas reivindicaciones 1 a 24 cumplen con el requisito de nivel inventivo, tal como se define en el artículo 18 de la Decisión 486 y como se explica

Clarke Modet

Carrera 11 No. 86-53, Piso 3
Edificio Segovia
110221 Bogotá, **Colombia**
T (+57) 1 618 10 88
F (+57) 1 635 08 24

detalladamente en el Manual Andino y la Guía para Examinadores de la Superintendencia de Industria y Comercio.

7. Conclusión

Con las modificaciones introducidas y los argumentos presentados puede concluirse que:

i) La presente solicitud es clara, concisa y está debidamente soportada en la descripción, cumpliendo con los requerimientos del Artículo 30 de la Decisión 486; y

ii) Las reivindicaciones actuales son patentables sobre D1 y D2, cumpliendo así con los requerimientos de los Artículos 16 y 18 de la Decisión 486.

Habiendo atendido cabalmente las objeciones presentadas por ese despacho, atentamente solicitamos se conceda el privilegio de patente de invención a la solicitud en estudio o si el señor examinador considera que subsisten razones para objetar la presente invención, rogamos expedir otro examen de fondo con los debidos motivos y razones que sustenten su objeción con el fin de que nuestro mandante tenga la posibilidad de exponer sus argumentos con base en la interpretación de los artículos 45 de la Decisión 486 -el cual otorga la facultad al examinador para emitir los exámenes de fondo- y 42 del Código de Procedimiento Administrativo y de lo Contencioso Administrativo que señala que: "*habiéndose dado oportunidad a los interesados para expresar sus opiniones, y con base en las pruebas e informes disponibles, se tomará la decisión, que <u>será motivada</u>. La decisión resolverá todas las peticiones que hayan sido oportunamente planteadas dentro de la actuación por el peticionario y por los terceros reconocidos*", (el subrayado es nuestro).

En consecuencia, solicitamos a ese Despacho pronunciarse en relación con todos los argumentos presentados en este memorial dando estricta aplicación al principio del debido proceso consagrado en el artículo 29 de la Constitución Nacional.

Clarke Modet

Carrera 11 No. 86-53, Piso 3
Edificio Segovia
110221 Bogotá, **Colombia**
T (+57) 1 618 10 88
F (+57) 1 635 08 24

8. Anexos

- Nuevo capítulo reivindicatorio conformado por veinticuatro (24) reivindicaciones.
- Artículo científico ("*Peptide-MHC-based nanomedicines for autoimmunity function as T-cell receptor microclustering devices*", *Nature Nanotechnology*, 2017 Julio; 12 (7): 701-710.

Señora Directora,

CAROLINA DAZA MONTALVO
C.C. 66.783.790 de Palmira Valle
TP-141563 CSJ
notificaciones@clarkemodet.com.co

REIVINDICACIONES

1. Un complejo que comprende un núcleo de nanopartículas acoplado a una pluralidad de complejos antígeno-MHC de clase II (pMHCII) relevantes para la enfermedad/inflamación autoinmune, en el que el núcleo de nanopartículas comprende hierro u óxido de hierro y tiene un diámetro de 1 nm a 100 nm; en el que la densidad de pMHCII relevante para la enfermedad autoinmune por área superficial de la nanopartícula es de 0,4 pMHC/100 nm^2 a 15 pMHC/100 nm^2 del área superficial de la nanopartícula; en el que los pMHCII se acoplan a un extremo funcionalizado con maleimida de un enlazador de polietilenglicol (PEG) que tiene menos de 5 kilodaltons de peso molecular, en el que un extremo no funcionalizado con maleimida del enlazador de polietilenglicol (PEG) está acoplado al núcleo de nanopartículas, y el extremo no funcionalizado con maleimida comprende un alcoxi, un alquilo, alquil-amida-alquilo, alquil-éster-alquilo, alquil-amida, alquil-ácido, o alquil-éster.

2. El complejo de reivindicación 1, en el que la molécula MHCII de la pluralidad de complejos pMHCII comprende HLA DR, HLA DQ, o HLA DP.

3. El complejo de reivindicación 2, en el que la molécula MHCII de la pluralidad de complejos pMHCII comprende HLA-DRB1/DRA, HLA-DRB3/DRA, HLA-DRB4/DRA, HLA-DRB5/DRA, HLA-DQA1/HLA-DQB1, o HLA-DPB1/HLA-DPA1.

4. El complejo de una cualquiera de las reivindicaciones 1 a 3, en el que el complejo comprende además una capa externa biocompatible, en el que dicha capa biocompatible comprende poli(etilenglicol).

5. El complejo de una cualquiera de las reivindicaciones 1 a 4, en el que la valencia de la pluralidad de complejos pMHCII por núcleo de nanopartículas es de 10:1 a 100:1.

6. El complejo de una cualquiera de las reivindicaciones 1 a 5, en el que el núcleo de la nanopartícula comprende un diámetro de 5 nm a 50 nm.

7. El complejo de una cualquiera de las reivindicaciones 1 a 6, en el que el antígeno para enfermedad/inflamación autoinmune se selecciona del grupo que consiste de:

a) un antígeno para la diabetes derivado de un antígeno seleccionado de uno o más del grupo: hInsB$_{10-18}$, hIGRP$_{228-236}$, hIGRP$_{265-273}$, IGRP$_{206-214}$, hIGRP$_{206-214}$, NRP-A7, NRP-I4, NRP-V7, YAI/D^{b}, INS B$_{15–23}$, PPI$_{76-90\ (K88S)}$, IGRP$_{13-25}$, GAD$_{555-567}$, GAD$_{555-567(557I)}$, IGRP$_{23-35}$, B$_{24}$-C$_{36}$, PPI$_{76-90}$, INS-I9, TUM, G6Pasa, Pro-insulina$_{L2-10}$, Pro-insulina$_{L3-11}$, Pro-insulina$_{L6-14}$, Pro-insulina$_{B5-14}$, Pro-insulina$_{B10-18}$, Pro-insulina$_{B14-22}$, Pro-insulina$_{B15-24}$, Pro-insulina$_{B17-25}$, Pro-insulina$_{B18-27}$, Pro-insulina$_{B20-27}$, Pro-insulina$_{B21-29}$, Pro-insulina$_{B25-C1}$, Pro-insulina$_{B27-C5}$, Pro-insulina$_{C20-28}$, Pro-insulina$_{C25-33}$, Pro-insulina$_{C29-A5}$, Pro-insulina$_{A1-10}$, Pro-insulina$_{A2-10}$, o Pro-insulina$_{A12-20}$;

b) un antígeno relevante para la esclerosis múltiple derivado de un antígeno seleccionado de uno o más del grupo: MOG$_{35-55}$, MOG$_{36-55,}$ MAG$_{287-295}$, MAG$_{509-517}$, MAG$_{556-564}$, MBP$_{110-118}$, MOG$_{114-122}$, MOG$_{166-175}$, MOG$_{172-180}$, MOG$_{179-188}$, MOG$_{188-196}$, MOG$_{181-189}$, MOG$_{205-214}$, PLP$_{80-88}$, MAG$_{287-295}$, MAG$_{509-517}$, MAG$_{556-564}$, MOG$_{97-109}$ MOG$_{97-109(E107S)}$, MBP$_{89-101}$, PLP$_{175-192}$, PLP$_{94-108}$, MBP$_{86-98}$, PLP$_{54-68}$, PLP$_{249-263}$, MOG$_{156-170}$, MOG$_{201-215}$, MOG$_{38-52}$, MOG$_{203-217}$, PLP$_{250-264}$, MPB$_{13-32}$, MPB$_{83-99}$, MPB$_{111-129}$, MPB$_{146-170}$, MOG$_{223-237}$, MOG$_{6-20}$, PLP$_{88-102}$, o PLP$_{139-154}$;

c) un antígeno relevante para la enfermedad celíaca derivado de un antígeno seleccionado de uno o más del grupo: aGlia$_{57-68}$, aGlia$_{62-72}$, o aGlia$_{217-229}$;

d) un antígeno relevante para la cirrosis biliar primaria derivado de un antígeno seleccionado de uno o más del grupo: PDC-E2$_{122-135}$, PDC-E2$_{249-262}$, PDC-E2$_{249-263}$, PDC-E2$_{629-643}$, PDC-E2$_{72-86}$, PDC-E2$_{353-367}$, PDC-E2$_{422-436}$, PDC-E2$_{629-643}$, PDC-E2$_{80-94}$, PDC-E2$_{353-367}$, o PDC-E2$_{535-549}$;

e) un antígeno relevante para pénfigo foliáceo y/o antígeno relevante para pénfigo vulgar, cada uno de los cuales se deriva de un antígeno seleccionado de uno o más del grupo: DG1$_{216-229}$, DG3$_{97-111}$, DG3$_{251-265}$, DG3$_{441-455}$, DG3$_{351-365}$, DG3$_{453-467}$, DG3$_{540-554}$, DG3$_{280-294}$, DG3$_{326-340}$, DG3$_{367-381}$, DG3$_{13-27}$, DG3$_{323-337}$, DG3$_{438-452}$, DG1$_{48-62}$, DG1$_{206-222}$, DG1$_{363-377}$, DG1$_{3-17}$, DG1$_{192-206}$, DG1$_{326-340}$, DG1$_{1-15}$, DG1$_{35-49}$, o DG1$_{325-339}$;

f) un antígeno relevante para el trastorno del espectro neuromielítico óptico derivado de un antígeno seleccionado de uno o más del grupo: AQP4$_{129-143}$, AQP4$_{284-298}$, AQP4$_{63-76}$, AQP4$_{129-143}$, o AQP4$_{39-53}$;

g) un antígeno relevante para el asma alérgica derivado de un antígeno seleccionado de uno o más del grupo: DERP1$_{16-30}$, DERP1$_{171-185}$, DERP1$_{110-124}$, DERP-2$_{26-40}$, o DERP-2 $_{107-121}$;

h) un antígeno relevante para la enfermedad intestinal inflamatoria derivado de un antígeno seleccionado de uno o más del grupo: bacteroides integrasa antígeno$_{183-197}$, bacteroides integrasa antígeno$_{146-160}$, bacteroides integrasa antígeno$_{175-189}$, bacteroides integrasa antígeno$_{1-15}$, bacteroides integrasa antígeno$_{183-197}$, bacteroides integrasa antígeno$_{30-44}$, bacteroides integrasa antígeno$_{70-84}$, bacteroides integrasa antígeno$_{337-351}$, bacteroides integrasa antígeno$_{171-185}$, bacteroides integrasa antígeno$_{4-18}$, bacteroides integrasa antígeno$_{256-270}$, Fla-2/Fla-X$_{366-380}$, Fla-2/Fla-X$_{164-178}$, Fla-2/Fla-X$_{261-275}$, Fla-2/Fla-X$_{1-15}$, Fla-2/Fla-X$_{51-65}$, Fla-2/Fla-X$_{269-283}$, Fla-2/Fla-X$_{4-18}$, Fla-2/Fla-X$_{271-285}$, YIDX$_{78-92}$, YIDX$_{93-107}$, YIDX$_{98-112}$, YIDX$_{23-37}$, YIDX$_{78-92}$, YIDX$_{195-209}$, YIDX$_{22-36}$, YIDX$_{80-94}$, o YIDX$_{101-115}$;

i) un antígeno relevante para el lupus eritematoso sistémico derivado de un antígeno seleccionado de uno o más del grupo: H4$_{71-94}$, H4$_{74-88}$, H4$_{76-90}$, H4$_{75-89}$, H4$_{78-92}$, H4$_{80-94}$, H2B$_{10-24}$, H2B$_{16-30}$, H1´$_{22-42}$, o H1´$_{27-41}$;

j) un antígeno relevante para la aterosclerosis derivado de un antígeno seleccionado de uno o más del grupo: ApoB$_{3501-3516}$, ApoB$_{1952-1966}$, ApoB$_{978-993}$, ApoB$_{3498-3513}$, ApoB$_{210A}$, ApoB$_{210B}$, o ApoB$_{210C}$;

k) un antígeno para EPOC y/o antígeno relevante para enfisema, cada uno de los cuales se deriva de un antígeno seleccionado de uno o más del grupo: elastina$_{89-103}$, elastina$_{698-712}$, elastina$_{8-22}$, elastina$_{94-108}$, elastina$_{13-27}$, elastina$_{695-709}$, elastina$_{563-577}$, elastina$_{558-572}$, elastina$_{698-712}$, elastina$_{566-580}$, o elastina$_{645-659}$;

l) un antígeno relevante para la psoriasis derivado de un antígeno seleccionado de uno o más del grupo: Cap18$_{64-78}$, Cap18$_{34-48}$, Cap18$_{47-61}$, Cap18$_{151-165}$, Cap18$_{149-163}$, Cap18$_{152-166}$, Cap18$_{131-145,}$ Cap$_{1824-38}$, ADMTSL5245$_{-259}$, ADMTSL5$_{267-281}$, ADMTSL5$_{372-386}$, ADMTSL5$_{289-303}$, ADMTSL5$_{396-410}$, ADMTSL5$_{433-447}$, ADMTSL5$_{142-156}$, ADMTSL5$_{236-250}$, ADMTSL5$_{301-315}$, ADMTSL5$_{203-217}$, o ADMTSL5$_{404-418}$;

m) un antígeno relevante para la hepatitis autoinmune derivado de un antígeno seleccionado de uno o más del grupo: CYP2D6$_{193-207}$, CYP2D6$_{76-90}$, CYP2D6$_{293-307}$, CYP2D6$_{313-332}$, CYP2D6$_{393-412}$, CYP2D6$_{199-213}$, CYP2D6$_{450-464}$, CYP2D6$_{301-315}$, CYP2D6$_{452-466}$, CYP2D6$_{59-73}$, CYP2D6$_{130-144}$, CYP2D6$_{193-212}$, CYP2D6$_{305-324}$, CYP2D6$_{131-145}$, CYP2D6$_{216-230}$, CYP2D6$_{238-252}$, CYP2D6$_{199-213}$, CYP2D6$_{235-252}$, CYP2D6$_{293-307}$, CYP2D6$_{381-395}$, CYP2D6$_{429-443}$, SLA$_{334-348}$,

$SLA_{196-210}$, $SLA_{115-129}$, $SLA_{373-386}$, $SLA_{186-197}$, $SLA_{317-331}$, $SLA_{171-185}$, $SLA_{417-431}$, $SLA_{359-373}$, $SLA_{215-229}$, $SLA_{111-125}$, $SLA_{110-124}$, $SLA_{299-313}$, $SLA_{342-356}$, SLA_{49-63}, $SLA_{119-133}$, $SLA_{260-274}$, SLA_{26-40}, SLA_{86-100}, o $SLA_{331-345}$;

n) un antígeno relevante para la uveítis derivado de un antígeno seleccionado de uno o más del grupo: $arrestina_{199-213}$, $arrestina_{77-91}$, $arrestina_{250-264}$, $arrestina_{172-186}$, $arrestina_{354-368}$, $arrestina_{239-253}$, $arrestina_{102-116}$, $arrestina_{59-73}$, $arrestina_{280-294}$, $arrestina_{291-306}$, $arrestina_{195-209}$, o $arrestina_{200-214}$;

o) un antígeno relevante para el síndrome de Sjogren derivado de un antígeno seleccionado de uno o más del grupo: $RO60_{127-141}$, $RO60_{523-537}$, $RO60_{243-257}$, $RO60_{484-498}$, $RO60_{347-361}$, $RO60_{369-383}$, $RO60_{426-440}$, $RO60_{267-281}$, $RO60_{178-192}$, $RO60_{358-372}$, $RO60_{221-235}$, $RO60_{318-332}$, $RO60_{407-421}$, $RO60_{459-473}$, $RO60_{51-65}$, $RO60_{312-326}$, $LA_{241-255}$, $LA_{101-115}$, $LA_{153-167}$, $LA_{178-192}$, LA_{19-33}, LA_{37-51}, $LA_{133-147}$, LA_{50-64}, LA_{32-46}, $LA_{153-167}$, LA_{83-97}, $LA_{136-150}$, $LA_{297-311}$, LA_{59-73}, $LA_{151-165}$, LA_{86-100}, o $LA_{154-168}$;

p) un antígeno relevante para la esclerodermia derivado de un antígeno seleccionado de uno o más del grupo: $TOP1_{346-360}$, $TOP1_{420-434}$, $TOP1_{750-764}$, $TOP1_{419-433}$, $TOP1_{591-605}$, $TOP1_{695-709}$, $TOP1_{305-319}$, $TOP1_{346-360}$, $TOP1_{419-433}$, $TOP1_{425-439}$, $TOP1_{614-628}$, $CENP\text{-}C_{297-311}$, $CENP\text{-}C_{857-871}$, $CENP\text{-}C_{887-901}$, $CENP\text{-}C_{212-226}$, $CENP\text{-}C_{643-657}$, $CENP\text{-}C_{832-846}$, $CENP\text{-}C_{167-181}$, $CENP\text{-}C_{246-260}$, $CENP\text{-}C_{846-860}$, $CENP\text{-}C_{149-163}$, $CENP\text{-}C_{833-847}$, o $CENP\text{-}C_{847-861}$;

q) un antígeno relevante para el síndrome antifosfolípido derivado de un antígeno seleccionado de uno o más del grupo: $APOH_{235-249}$, $APOH_{306-320}$, $APOH_{237-251}$, $APOH_{295-309}$, $APOH_{28-42}$, $APOH_{173-187}$, $APOH_{264-278}$, $APOH_{295-309}$, $APOH_{49-63}$, $APOH_{269-283}$, $APOH_{295-309}$, $APOH_{321-355}$, $APOH_{322-336}$, o $APOH_{324-338}$;

r) un antígeno relevante para vasculitis asociado a ANCA derivado de un antígeno seleccionado de uno o más del grupo: $MPO_{506-520}$, $MPO_{302-316}$, MPO_{7-21}, $MPO_{689-703}$, $MPO_{248-262}$, $MPO_{444-458}$, $MPO_{513-527}$, MPO_{97-111}, $MPO_{616-630}$, $MPO_{462-476}$, $MPO_{617-631}$, $MPO_{714-728}$, $PRTN3_{44-58}$, $PRTN3_{234-248}$, $PRTN3_{59-73}$, $PRTN3_{117-131}$, $PRTN3_{164-178}$, $PRTN3_{71-85}$, $PRTN3_{241-255}$, $PRTN3_{59-73}$, $PRTN3_{183-197}$, $PRTN3_{62-76}$, $PRTN3_{118-132}$, o $PRTN3_{239-253}$; o

s) un antígeno relevante para el síndrome del hombre rígido derivado de un antígeno seleccionado de uno o más del grupo: $GAD_{212-226}$, $GAD_{555-569}$, o $GAD_{297-311}$.

8. Una composición que comprende una pluralidad de complejos de cualquiera de las reivindicaciones 1 a 7 y un portador farmacéuticamente aceptable.

9. Un complejo que comprende un núcleo de nanopartículas acoplado a una pluralidad de complejos antígeno-MHC de clase II (pMHCII) para diabetes de tipo I, en el que el núcleo de nanopartículas comprende un metal u óxido de metal y tiene un diámetro de 1 nm a 100 nm; en el que la densidad de pMHCII para la diabetes de tipo I por nanopartícula es de 0,4 pMHC/100 nm^2 a 15 pMHC/100 nm^2 del área superficial de la nanopartícula, en el que los pMHCII se acoplan a un extremo funcionalizado con maleimida de un enlazador de polietilenglicol (PEG) que tiene menos de 5 kilodaltons de peso molecular, en el que un extremo no funcionalizado con maleimida del enlazador de polietilenglicol (PEG) está acoplado al núcleo de nanopartículas, y el extremo no funcionalizado con maleimida comprende un alcoxi, un alquilo, alquil-amida-alquilo, alquil-éster-alquilo, alquil-amida, alquil-ácido, o alquil-éster.

10. El complejo de la reivindicación 9, en el que la molécula MHCII de la pluralidad de los complejos pMHCII comprende HLA DR, HLA DQ, o HLA DP.

11. El complejo de la reivindicación 10, en el que la molécula MHCII de la pluralidad de los complejos pMHCII comprende HLA-DRB1/DRA, HLA-DRB3/DRA, HLA-DRB4/DRA, HLA-DRB5/DRA, HLA-DQA1/HLA-DQB1, o HLA-DPB1/HLA-DPA1.

12. El complejo de una cualquiera de las reivindicaciones 9 a 11, en el que el complejo comprende además una capa externa biocompatible, en el que dicha capa biocompatible comprende poli(etilenglicol).

13. El complejo de una cualquiera de las reivindicaciones 9 a 12, en el que la valencia de la pluralidad de complejos pMHCII por núcleo de nanopartículas es de 10:1 a 100:1.

14. El complejo de una cualquiera de las reivindicaciones 9 a 13, en el que el núcleo de nanopartículas comprende un diámetro de 5 nm a 50 nm.

15. El complejo de una cualquiera de las reivindicaciones 9 a 14, en el que el núcleo de nanopartículas comprende un diámetro de 5 nm a 25 nm.

16. El complejo de una cualquiera de las reivindicaciones 9 a 15, en el que el antígeno relevante para diabetes tipo I se selecciona del grupo que comprende: uno o más de preproinsulina (PPI), glucosa-6-fosfatasa específica de islote (IGRP), glutamato descarboxilasa (GAD), autoantígeno-2 de célula de islote (ICA2), insulina, o proinsulina.

17. El complejo de una cualquiera de las reivindicaciones 9 a 15, en el que los complejos antígeno-pMHCII para la diabetes de tipo I se seleccionan del grupo que comprende: $PPI_{76\text{-}90(K88S)}$-HLA-DRB1*0401/DRA, $IGRP_{13\text{-}25}$-HLA-DRB1*0301/DRA, $GAD_{555\text{-}567}$-HLA-DRB1*0401/DRA, $GAD_{555\text{-}567(557I)}$-HLA-DRB1*0401/DRA, $IGRP_{23\text{-}35}$-HLADRB1*0401/DRA, B_{24}-C_{36}-HLA-DRB1*0301/DRA, or PPI76-90-HLA-DRB1*0401/DRA.

18. El complejo de acuerdo con la reivindicación 17, en el que los complejos antígeno-pMHCII para la diabetes tipo I comprenden $PPI_{76\text{-}90(K88S)}$-HLA-DRB1*0401/DRA or $IGRP_{13\text{-}25}$-HLA-DRB1*0301/DRA.

19. Una composición que comprende una pluralidad de complejos de la reivindicación 18 y un portador farmacéuticamente aceptable.

20. El complejo de cualquiera de las reivindicaciones 1 a 8, en el que el antígeno para la enfermedad/inflamación autoinmune se selecciona de la lista que consiste en un antígeno para la diabetes, un antígeno para la esclerosis múltiple, un antígeno para la enfermedad celíaca, un antígeno para la cirrosis biliar primaria, un antígeno para el pénfigo foliáceo, un antígeno para el trastorno del espectro neuromielítico óptico, un antígeno para el asma alérgica, un antígeno para la enfermedad inflamatoria del intestino, un antígeno para el lupus eritematoso sistémico, un antígeno para aterosclerosis, un antígeno para la EPOC y/o un antígeno para el enfisema, un antígeno para la psoriasis, un antígeno para la hepatitis autoinmune, un

antígeno para la uveítis, un antígeno para el síndrome de Sjogren, un antígeno para la esclerodermia, un antígeno para el síndrome de fosfolípidos, un antígeno para la vasculitis asociado con ANCA, y un antígeno para el síndrome del hombre rígido.

21. El complejo de cualquiera de las reivindicaciones 1 a 8, 9 a 18, o 20, en el que el extremo no funcionalizado con maleimida comprende un alcoxi o un alquilo.

22. El complejo de la reivindicación 21, en el que el extremo no funcionalizado con maleimida comprende un alcoxi.

23. El complejo de la reivindicación 22, en el que el alcoxi comprende alquilo C_1 a C_3.

24. El complejo de la reivindicación 21, en el que el extremo no funcionalizado con maleimida comprende un alquilo.

nature nanotechnology

ARTICLES

PUBLISHED ONLINE: 24 APRIL 2017 | DOI: 10.1038/NNANO.2017.56

Peptide–MHC-based nanomedicines for autoimmunity function as T-cell receptor microclustering devices

Santiswarup Singha[1†], Kun Shao[1†], Yang Yang[1,2*], Xavier Clemente-Casares[1], Patricia Solé[3], Antonio Clemente[3], Jesús Blanco[3], Qin Dai[4], Fayi Song[4], Shang Wan Liu[5], Jun Yamanouchi[1], Channakeshava Sokke Umeshappa[1], Roopa Hebbandi Nanjundappa[1], Pascal Detampel[6], Matthias Amrein[6], César Fandos[3], Robert Tanguay[7], Susan Newbigging[8], Pau Serra[3], Anmar Khadra[5], Warren C. W. Chan[4] and Pere Santamaria[1,3*]

We have shown that nanoparticles (NPs) can be used as ligand-multimerization platforms to activate specific cellular receptors *in vivo*. Nanoparticles coated with autoimmune disease-relevant peptide-major histocompatibility complexes (pMHC) blunted autoimmune responses by triggering the differentiation and expansion of antigen-specific regulatory T cells *in vivo*. Here, we define the engineering principles impacting biological activity, detail a synthesis process yielding safe and stable compounds, and visualize how these nanomedicines interact with cognate T cells. We find that the triggering properties of pMHC–NPs are a function of pMHC intermolecular distance and involve the sustained assembly of large antigen receptor microclusters on murine and human cognate T cells. These compounds show no off-target toxicity in zebrafish embryos, do not cause haematological, biochemical or histological abnormalities, and are rapidly captured by phagocytes or processed by the hepatobiliary system. This work lays the groundwork for the design of ligand-based NP formulations to re-program *in vivo* cellular responses using nanotechnology.

We have demonstrated that systemic delivery of NPs coated with autoimmune disease-relevant pMHC class I (ref. 1) or class II ligands[2] results in the expansion of disease-suppressing (regulatory) T lymphocytes *in vivo*. Specifically, treatment of spontaneously diabetic non-obese diabetic (NOD) mice or C57BL/6 mice affected with experimental autoimmune encephalomyelitis (EAE, a model of multiple sclerosis) or collagen-induced arthritis (a model of rheumatoid arthritis) with mono-specific pMHC class I or class II-coated NPs triggered the expansion of cognate regulatory $CD8^+$ or $CD4^+$ T cells, and restored normoglycemia in diabetic mice or motor function in paralytic EAE mice and resolved joint inflammation in arthritic mice[2].

This therapeutic avenue exploits a new immunological paradigm whereby disease-specific autoreactive effector/memory T cells differentiate into regulatory T (Treg) cells and undergo profound expansions in response to systemic pMHC–NP therapy. According to this paradigm, any single pMHC specificity targeted in an autoimmune disease should be able, when coated as a ligand onto NPs, to selectively blunt autoimmune responses without impairing normal immunity. In agreement with this, the 20 disease-relevant pMHC–NPs tested so far have shown similar efficacy, regardless of disease model, prevalence, or role in the disease. The NP component is an essential ingredient of the final drug product, rather than a vehicle for antigen delivery[1–3].

Remarkably, pMHC-based nanomedicines can expand antigen-specific regulatory T cells *in vivo* to levels that are several-hundred-fold higher than the numbers of *in vitro*-expanded regulatory T cells that can afford clinical responses in patients on transfusion[4,5]. The efficacy of this approach is complemented by a well-defined mechanism of action, and availability of a true biomarker of therapeutic efficacy (expansion of autoregulatory T cells in blood)[1,2]. However, bench-to-bedside translation of pMHC–NP-based immunotherapy as well as application of this approach to trigger receptors on other cells types *in vivo* will require a detailed understanding of the physical/chemical parameters impacting pharmacodynamics. Here, we define the key synthesis variables, simplify manufacturing, discover critical roles for ligand density in therapeutic efficacy and elucidate the mode of binding to cognate T cells. We have engineered a novel biocompatible pMHC–NP design that offers a powerful new tool to expand regulatory T-cell memory to treat inflammatory disorders, and to build next-generation ligand-based nanomedicines.

[1]Julia McFarlane Diabetes Research Centre (JMDRC) and Department of Microbiology, Immunology and Infectious Diseases, Snyder Institute for Chronic Diseases and Hotchkiss Brain Institute, Cumming School of Medicine, University of Calgary, Calgary, Alberta T2N 4N1, Canada. [2]Department of Biochemistry and Molecular Biology, Cumming School of Medicine, University of Calgary, Calgary, Alberta T2N 4N1, Canada. [3]Institut D'Investigacions Biomèdiques August Pi i Sunyer, Barcelona 08036, Spain. [4]Institute of Biomaterials and Biomedical Engineering, Departments of Chemistry, Chemical Engineering, and Materials Sciences and Engineering, Donnelly Centre for Cellular and Biomolecular Research, University of Toronto, 164 College Street, Toronto, Ontario M5S 3G9, Canada. [5]Department of Physiology, McGill University, McIntyre Medical Building, Montreal, Quebec H3G 1Y6, Canada. [6]Departments of Cell Biology and Anatomy, and Pathology & Laboratory Medicine, Faculty of Medicine, University of Calgary, Calgary, Alberta T2N 4N1, Canada. [7]Environmental & Molecular Toxicology Sinnhuber Aquatic Research Laboratory, Oregon State University, Corvalis, Oregon 97333, USA. [8]Center for Modeling Human Disease, Toronto Centre for Phenogenomics, Lunenfeld Research Institute, 25 Orde Street, Toronto, Ontario M5T 3H7, Canada. [†]These authors contributed equally to this work. *e-mail: yyang@ucalgary.ca; psantama@ucalgary.ca

© 2017 Macmillan Publishers Limited, part of Springer Nature. All rights reserved.

Novel NP design with high pMHC-binding capacity

To define the key parameters governing pMHC–NP functionality, we first coated multiple copies of the type 1 diabetes (T1D)-relevant NRP-V7/K^d pMHC class I, expressed either as a single-chain complex in chinese hamster ovary (CHO) cells or as a two-chain complex in bacteria, onto gold NPs (GNPs) (Supplementary Fig. 1a,b and Supplementary Table 1). We confirmed that the biological activity of pMHC–NPs was a function of pMHC-binding capacity (not shown).

To facilitate clinical translation, we next focused on iron oxide-based pMHC–NPs. Small iron oxide (Fe_3O_4) NPs were generated via thermal decomposition of iron(III)acetylacetonate in the presence of surfactants[6], then stablized and functionalized by the addition of dopamine-polyethylene-glycol (DPA-PEG) linkers (Supplementary Table 1). High pMHC valencies were obtained using carboxyl (–COOH)- or primary amine (–NH_2)-functionalized NPs (SFP-C or SFP-N). The use of DPA-PEG linkers amenable to pMHC ligation via click chemistry (SFP-Z, carrying azide groups), or disulfide bonds (SFP-M or SFP-O, employing maleimide or orthopyridyl-disulfide groups) (Fig. 1a) did not improve pMHC binding capacity or compound stability (Supplementary Tables 1 and 2, and Supplementary Fig. 1a,b).

To overcome these limitations and the need to use surfactants, we sought to produce functionalized water-soluble NPs in a single-step thermal decomposition reaction of iron(III)acetylacetonate in the presence of functionalized PEG linkers (Fig. 1a and Supplementary Table 1). As shown in Supplementary Table 2, this reaction yielded Fe_3O_4 NPs larger than SFP-NPs, referred to as PF-C (carboxyl), PF-N (amine) and PF-M (maleimide); no NPs formed when using methoxy-PEG-orthopyridyl disulfide (Supplementary Tables 1 and Table 2). Figure 1 shows representative transmission electron microscopy (TEM) (Fig. 1b) and dynamic light scattering (DLS) profiles (Fig. 1c) of the productive designs, as well as an image of small angle electron beam diffraction (SEBD) (Fig. 1d) documenting the Fe_3O_4 nature of the iron oxide core. Agarose gel electrophoresis suggested that the reaction did not compromise the structural integrity of the functional groups of the PEGs, based on the expected effects of these groups on electrophoretic mobility (Fig. 1e). Fourier transform infrared spectroscopy (FTIR) analysis demonstrated the presence of the PEG backbone on all three types of PF-NP, as well as the structural integrity of the carboxyl, primary amine and maleimide groups (Fig. 1f). Each of these NP types had superior pMHC binding capacity than the corresponding SFP designs, particularly PF-M (Supplementary Table 2). PF-M NPs enabled directional conjugation of pMHC via the carboxyterminal cysteine (Cys) (Supplementary Fig. 1a) and magnetic purification from unconjugated pMHCs. Native and denaturing polyacrylamide gel electrophoresis (PAGE) analysis of pMHC class I/II-conjugated PF-M (Fig. 1g,h and Supplementary Fig. 1c) confirmed that virtually all pMHC was covalently coupled to the NPs. As expected, the pMHC-coated NPs had a slightly bigger hydrodynamic diameter than unconjugated NPs (Fig. 1i) and were structurally and functionally stable for up to 12 months of storage in phosphate-buffered saline (PBS) at 4 °C (Supplementary Fig. 1d–g).

pMHC density on the NP plays a critical role

We compared the ability of various NRP-V7/K^d-NP preparations to activate cognate 8.3-$CD8^+$ T cells (NRP-V7/$IGRP_{206-214}$-specific). Surprisingly, 8.3-$CD8^+$ T cells produced substantially higher amounts of interferon-gamma (IFNγ) in response to SFP-NPs carrying as few as 11 pMHCs per NP than in response to SFP-NPs carrying 8 pMHCs per NP, over a broad range of pMHC–NP or pMHC concentrations (Fig. 2a). This suggested that there is a threshold of pMHC valency for agonistic activity of SFP-NPs, lying between 9 and 11 pMHCs per NP, below which increases in NP concentration cannot overcome low agonistic activity (Fig. 2a,b).

To confirm this observation, we used PF-NPs, which are larger than SFP-NPs and thus have greater pMHC-coating capacity. pMHC-PF NPs carrying 13 or fewer pMHCs per NP had very weak or no biological activity up to $\sim 8 \times 10^{12}$ NPs ml^{-1}, as compared to PF-NPs displaying a much higher pMHC valency (61 pMHCs per NP; Fig. 2c,d). This supported the idea that the threshold of pMHC required for agonistic activity increases with NP size (that is, from >8 pMHCs for ~8 nm SFP-NPs to >13 pMHCs for ~20 nm PF-NPs), suggesting a role for pMHC density. This is further illustrated in Fig. 2e,f, where we compare the biological activity of SFP- and PF-NPs coated with a similar number of pMHCs over a range of NP or pMHC concentrations.

We compared the maximum binding capacities and predicted threshold valencies of NPs of different sizes, to identify a pMHC-density threshold (Supplementary Table 3). The theoretical pMHC density threshold lies at 0.004468 pMHCs nm^{-2}, corresponding to 11 pMHCs for an 8 nm NP or 22 pMHCs for a 20 nm NP (a calculated intermolecular distance of ~16.88 nm). The estimated width of the T-cell antigen receptor (TCR) complex[7,8] based on 3D reconstruction (~12 nm)[9] is consistent with the calculated inter-pMHC distance of 16.88 nm to reach the agonistic threshold. We calculate the minimum possible intermolecular distance at ~3.62 nm, which bodes well with the estimated 3–6 nm distance spanning individual TCRs within TCRαβ nanoclusters; this distance would allow a near-perfect alignment of pMHC on the NPs and cognate TCRs on T cells (Supplementary Fig. 2a).

These hypothetical predictions based on data generated using pMHC class I-coated NPs were tested by comparing the TCR triggering potency of PF-NPs coated with pMHC class II monomers, over a broad range of valencies. $CD4^+$ T cells isolated from BDC2.5-TCR-transgenic NOD mice produced small amounts of IFNγ in response to PF-M NPs coated with up to 22 cognate (BDC2.5mi/IA^{g7}) pMHCs (0.0045 pMHCs nm^{-2}; Fig. 2g). Remarkably, by plotting the IFNγ secretion data obtained at 10 and 5 μg of pMHC ml^{-1} (the concentrations at which the dose response effect plateaus), we see that the magnitude of IFNγ secretion increases exponentially in response to relatively small increases in pMHC valency, starting at ~22 pMHCs (the predicted threshold valency) and ending at ~32 pMHCs per NP (0.0065 pMHCs nm^{-2}, herein referred to as the 'minimal optimal valency') (Fig. 2h). Substantial increases in pMHC valency/density above this minimal optimal valency do not result in significantly higher potency (Fig. 2h).

To ascertain if these biological effects were due to differences in TCR signalling, we transduced the Jurkat/MA (JurMA) human T-cell line (carrying a luciferase reporter driven by nuclear factor of activated T-cells (NFAT)-binding DNA)[10] with lentiviruses encoding the BDC2.5 TCRαβ and murine CD4. As shown in Fig. 2i, BDC2.5-TCR/mCD4-JurMA cells responded rapidly (within 2 h), vigorously and for a sustained period of time (>24 h) to BDC2.5mi/IA^{g7}-coated PF-M, as compared with optimal concentrations of an agonistic anti-human CD3ε mAb or phorbol 12-myristate 13-acetate (PMA)/ionomycin, which triggered a much slower response that peaked at 14 h and progressively decreased afterwards. Notably, experiments using PF-M NPs coated with a broad range of BDC2.5mi/IA^{g7} valencies indicated that the magnitude of luciferase expression (a direct read-out of TCR signalling) followed kinetics similar to those seen with primary BDC2.5-$CD4^+$ T cells, indicating that threshold and supra-threshold pMHC densities somehow promote cooperative TCR signalling (Fig. 2j).

In silico–in vivo modelling experiments based on the *in vitro* data and the scheme shown in Fig. 3a suggested that both pMHC density and dose play significant roles in the regulatory T cell re-programming and/or expanding properties of these compounds *in vivo* (Fig. 3b–d). To test these predictions, we compared the type-1 regulatory

© 2017 Macmillan Publishers Limited, part of Springer Nature. All rights reserved.

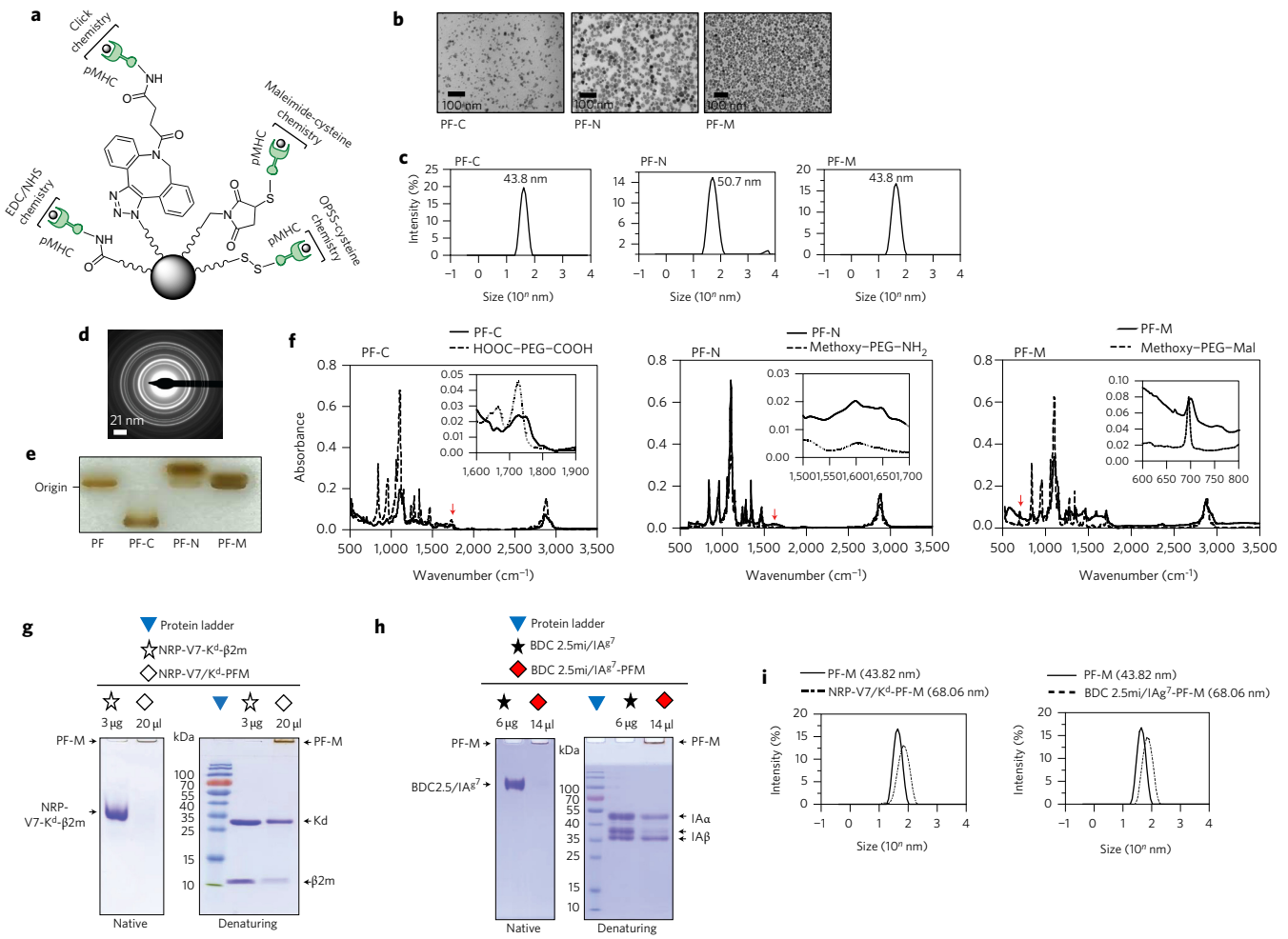

Figure 1 | Biophysical characterization of pMHC–PF. a, Cartoon depicting NPs conjugated with pMHCs using the four different chemistries tested. OPSS, orthopyridyl disulfide. **b**,**c**, TEM images (**b**) and DLS profiles (**c**) of PF-C, PF-N and PF-M. **d**, Representative SEBD analysis of PF-M. **e**, Agarose gel electrophoretic patterns of PF, PF-C, PF-N and PF-M. **f**, FTIR profiles of PF-C, PF-N and PF-M. The dotted lines correspond to the FTIR profiles of COOH–PEG–COOH, mPEG–NH_2 and mPEG–maleimide. The peaks at 2,883 cm^{-1} (C–H asymmetric stretching vibration), 1,106 cm^{-1} (C–O–C vibration) and 958–960 cm^{-1} (CH_2 rocking vibration) indicated the presence of PEG on all three NP types. Red arrows identify the signature signals (enlarged in insets) of the carboxyl, NH_2 and maleimide groups. The reduced signal strength of C=O stretching vibration at 1,728 cm^{-1} of COOH on PF-C is likely to be due to binding of some COOH groups to NPs. The unaltered primary amine (NH_2) bending vibration at 1,606 cm^{-1} and the C=O of maleimide in-plane bending vibration at 696 cm^{-1} indicated that these groups are exposed. **g**,**h**, Native and denaturing PAGE of NRP-V7/K^d-PF-M (**g**) and BDC2.5mi/IA^{g7}-PF-M (**h**) versus soluble pMHCs. **i**, DLS profiles for unconjugated (solid) and pMHC-conjugated PF-M (dashed line).

T (TR1) cell expanding properties[2] using various preparations of PF-NPs coated with BDC2.5mi/IA^{g7} pMHCs at minimal optimal densities or higher (as defined *in vitro*, corresponding to 29–59 pMHCs per NP). These experiments demonstrated pMHC dose-dependent effects within individual preparations, but also no significant effects of pMHC valency across preparations (Fig. 3e,f and Supplementary Fig. 3a). Surprisingly, however, studies using the smaller BDC2.5mi-IA^{g7}-SFP-NPs carrying 22–44 pMHCs per NP indicated significantly higher TR1 expanding effects, at all doses tested, than BDC2.5mi-IA^{g7}-PF-NPs carrying 29–45 pMHCs per NP (Supplementary Fig. 3b). These seemingly counterintuitive observations suggested that, besides dose, pMHC densities greater than the minimal optimal density do somehow enhance Treg cell formation and/or expansion. These results were further substantiated by producing small (11 nm) PF-NPs and testing the ability of their BDC2.5mi-IA^{g7}-coated counterparts to expand cognate TR1 cells *in vivo* (data not shown).

We have shown that class II pMHC–NP therapy triggers (1) the conversion of TR1-poised effector/memory T cells into TR1 cells by promoting the expression of IL-10 mRNA and the upregulation of CD49b; and (2) the subsequent expansion of these re-programmed TR1 cells[2]. We therefore reasoned that pMHC density might regulate the efficiency of TR1 cell formation, whereas dose might control the magnitude of TR1 cell expansion. To investigate this, we measured the effects of dose and pMHC density (above the minimal optimal density) on the levels of CD49b expressed by the cognate (tetramer$^+$) TR1-like $CD4^+$ cells arising in response to therapy. Interestingly, we found a statistically significant correlation between BDC2.5mi/IA^{g7} density and the magnitude of CD49b upregulation on these cells; this effect peaked at ~0.012 pMHC nm^{-2} (equivalent to 60 pMHC on a 20 nm PF-NP) (Fig. 3g). Interestingly, pMHC dose had a minor, non-statistically significant effect on this phenotype (Fig. 3h), despite its clear effect on the TR1-expanding properties of these nanomedicines (Fig. 3e). Thus, pMHC density and pMHC dose have separate roles in promoting Treg conversion and expansion, respectively.

pMHC–NPs trigger sustained TCR microcluster formation

Since pMHC–NPs promote Treg cell conversion by directly ligating TCRs on cognate T cells[2], the above results suggested that pMHC–NPs operate by inducing prolonged TCR ligation.

© 2017 Macmillan Publishers Limited, part of Springer Nature. All rights reserved.

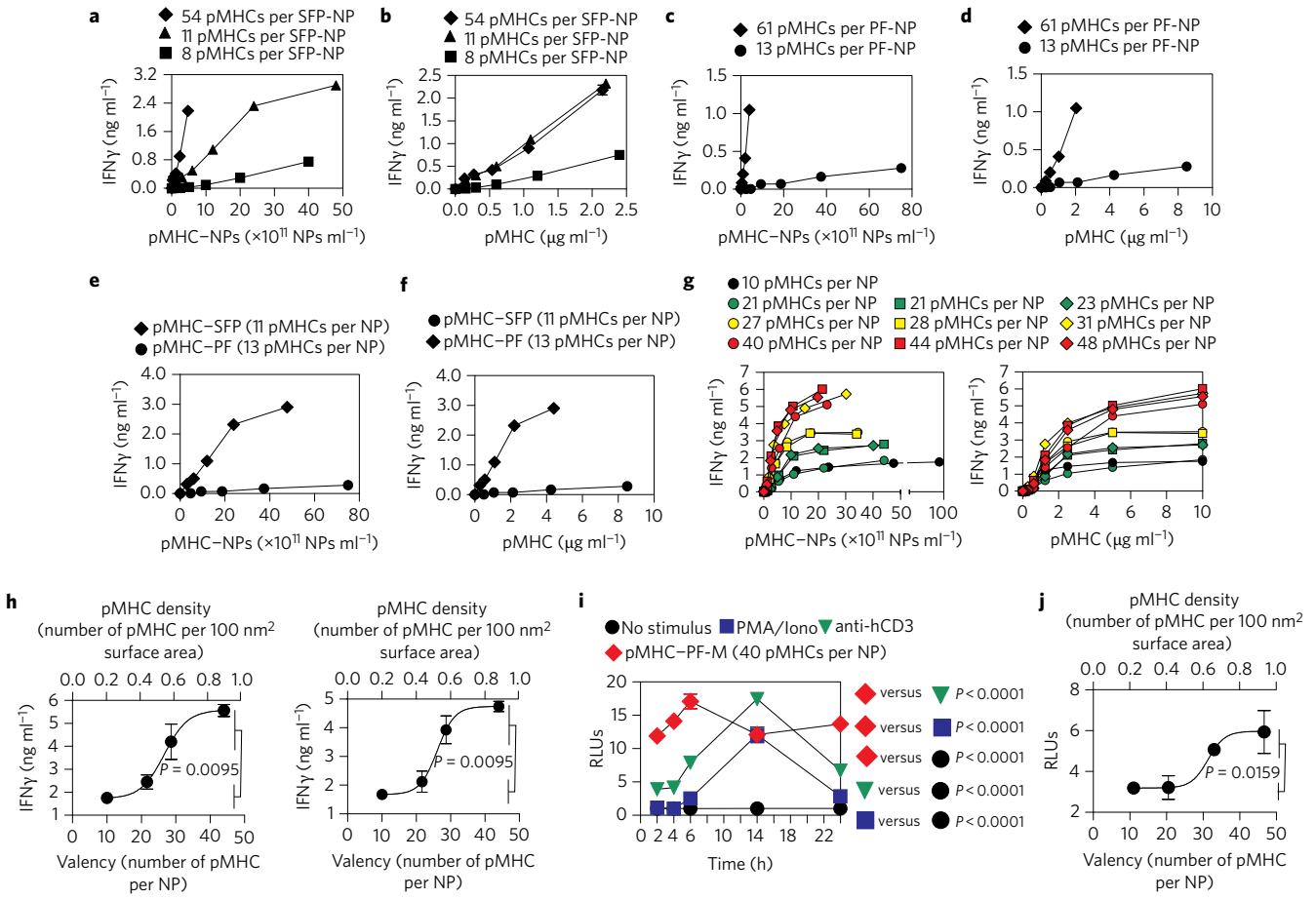

Figure 2 | Effects of NP size and pMHC valency on T-cell agonistic activity and TCR signalling. a, Production of IFNγ by 8.3-CD8$^+$ T cells in response to NRP-V7/K^d-SFP as a function of pMHC valency and NP numbers. **b**, Agonistic properties of the NRP-V7/K^d-SFPs from **a**, as a function of pMHC concentration in the assay. **c**,**d**, Production of IFNγ by 8.3-CD8$^+$ T cells in response to PF conjugated with two different NRP-V7/K^d valencies, as a function of pMHC–NP (**c**) or pMHC concentration in the assay (**d**). **e**,**f**, Comparison of the agonistic properties of small (SFP) versus larger (PF) NPs coated with low NRP-V7/K^d valencies, as a function of pMHC–NP (**e**) or pMHC concentration (**f**). Data in **a**–**f** correspond to the average ± s.e.m. values of IFNγ secretion in triplicate wells (error bars were usually smaller than the size of the symbols used to display the data) and each panel corresponds to one representative experiment out of at least three independent experiments. Negative controls involved the use of unconjugated or Cys-conjugated NPs at the highest concentration of NPs (that is, 50×10^{11} NPs ml^{-1} in **a**), yielding zero IFNγ values. **g**, Comparison of the agonistic properties of PF NPs conjugated with 10 different BDC2.5mi/IA^{g7} valencies on BDC2.5-CD4$^+$ T cells, as a function of pMHC–NP (left) or pMHC concentration (right). Data shown correspond to one experiment. Data for 5 and 10 μg of pMHC were repeated twice more with similar results. As a negative control, we used Cys-conjugated NPs at a concentration of iron equivalent to that corresponding to 10 μg pMHC ml^{-1} of the 10 pMHC per NP preparation (95×10^{11} NPs ml^{-1}), yielding zero IFNγ values. **h**, Relationship between BDC2.5 mi/IA^{g7} valency and density on PF NPs (grouped according to sub-threshold, threshold, minimal optimal and supra-threshold densities) and agonistic activity on BDC2.5-CD4$^+$ T cells at 10 μg ml^{-1} (left) and 5 μg ml^{-1} (right) (concentrations of pMHC yielding near-maximal agonistic activity). *P* values between sub-threshold/threshold versus minimal optimal valency/supra-threshold valencies were calculated via a Mann–Whitney U test. **i**, Luciferase activity (average ± s.e.m. of triplicates) in BDC2.5-TCR/mCD4/NFAT-luciferase-expressing JurMA cells in response to stimulation for various periods of time with BDC2.5mi/IA^{g7}-PF-M (12.5 μg ml^{-1}), soluble anti-hCD3ε mAb (10 μg ml^{-1}) and PMA/ionomycin. RLU, relative light units. As a negative control, we used Cys-conjugated NPs at a concentration of iron equivalent to that corresponding to 5 μg pMHC ml^{-1} of the 10 pMHC per NP preparation (45.5×10^{11} NPs ml^{-1}), yielding 1.05 RLUs. Data shown are representative of at least three independent experiments per stimulation condition. *P* values between conditions were calculated via two-way ANOVA. **j**, Relationship between BDC2.5mi/IA^{g7} valency and density on PF NPs (grouped according to sub-threshold, threshold, minimal optimal and supra-threshold densities) and agonistic activity on BDC2.5-TCR/mCD4/NFAT-luciferase-expressing JurMA cells at 5 μg ml^{-1}. *P* values were calculated via a Mann–Whitney U test.

It has been shown that, on naive T cells, TCRs are organized as linear clusters[11] or nonlinear assemblies[12] of up to ~200 nm in diameter/length (nanoclusters)[13], and that pMHC ligation promotes the formation of TCR microclusters ranging from 300 to 800 nm (refs 12,14–16). To gain insights into the pMHC density effect described above, we investigated the geometry and kinetics of pMHC–NP binding to cognate T cells. TEM studies revealed that pMHC–NPs bind CD8$^+$ or CD4$^+$ T cells as clusters of several NPs spanning ~100–150 nm (Fig. 4a,b). This binding geometry was already seen within 30 min at 4 °C, was followed by cluster growth (to ~400 nm) on incubation at 37 °C (Fig. 4a,b,g), and culminated in internalization of the NPs in intracellular vesicles, starting ~3 h after binding (Fig. 4a,b). This clustered engagement was antigen-specific as neither binding nor internalization were seen when pMHC–NPs were incubated with non-cognate T cells (Fig. 4c). These results were substantiated by super-resolution microscopy (Fig. 4d) and scanning electron microscopy (SEM) (Supplementary Fig. 4a,b). Thus, pMHC–NPs function as TCR nanocluster-binding and microcluster-triggering devices.

As Treg conversion is a direct function of pMHC density, we investigated whether variations in pMHC density had any effects

© 2017 Macmillan Publishers Limited, part of Springer Nature. All rights reserved.

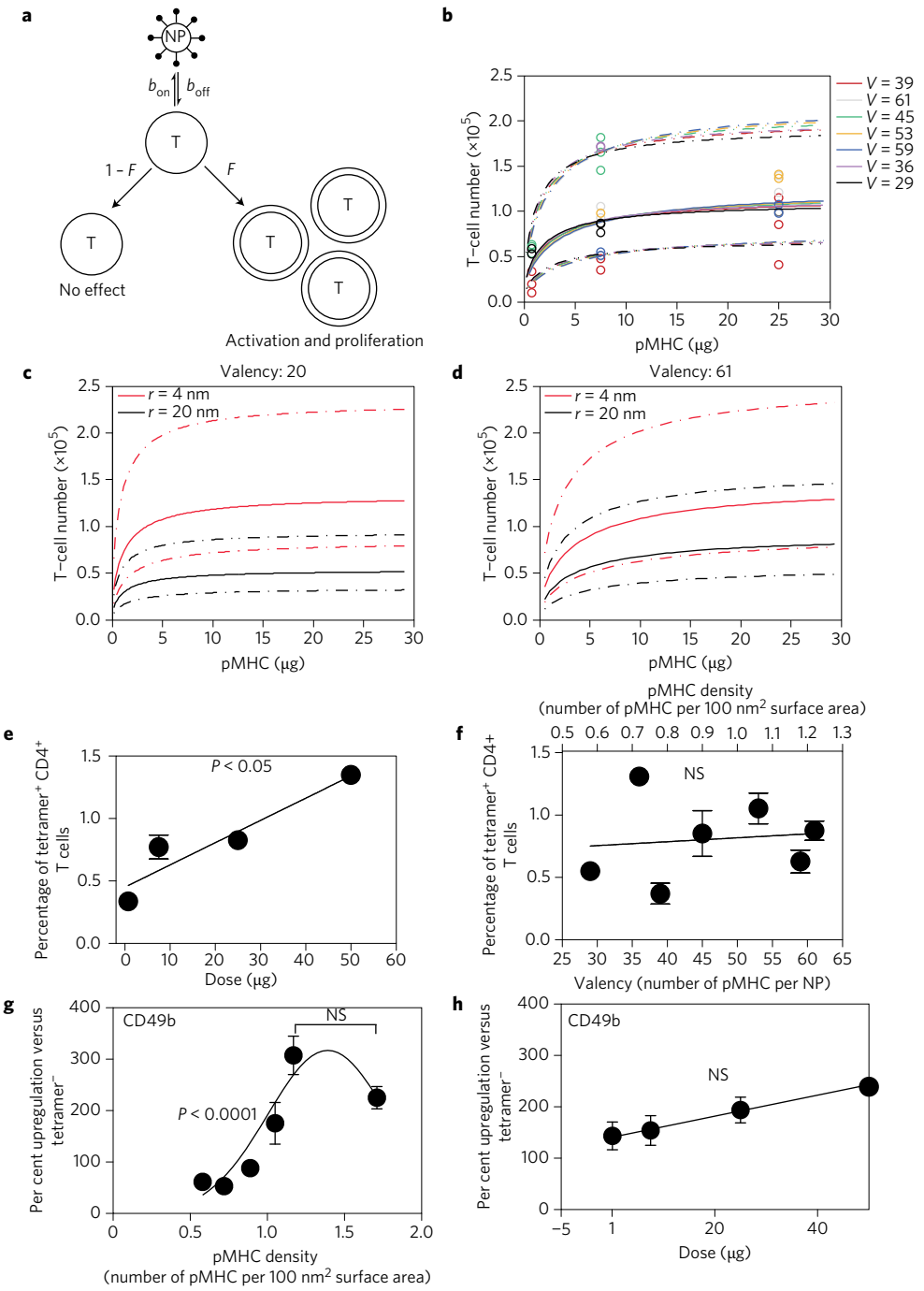

Figure 3 | Autoregulatory T-cell expansion properties of BDC2.5mi/IA^{g7}-PF-M *in vivo* versus pMHC valency/density and dose. a, Schematic diagram delineating the mathematical model of NP-dependent T-cell expansion. NP binding to T cells with an affinity K causes a fraction, F, of T cells to become activated and proliferative, and a fraction, $1 - F$, to remain unaffected. b_{on}, binding association rate constant; b_{off}, binding dissociation rate constant. **b**, Model simulations of the number of free or unbound T cells (that is, X) as a function of the total pMHC expression level on NPs (V) fitted to experimental data of T-cell expansion induced by injecting 20 nm NPs (see **e**). Solid lines are the mean and dashed-dotted lines are the 90% confidence envelopes. **c**,**d**, Comparison of the simulated number of T cells in response to injections by NPs of radius (r) of 4 nm versus 20 nm coated with 20 (**c**) or 61 (**d**) pMHCs per NP. Solid lines are the mean and dashed-dotted lines are the 90% confidence envelopes. **e**, Relationship between the percentages of 2.5mi/IA^{g7} tetramer$^+$ cells in splenic CD4$^+$ T cells of 10-week-old NOD mice treated with 10 injections of 7 different BDC2.5mi/IA^{g7}-PF-M preparations (displaying 29, 36, 39, 45, 53, 59 and 61 pMHC valencies, respectively) as a function of pMHC amount per dose (0.75, 7.5, 25 and 50 μg of pMHC per dose, and $n = 8$, 16, 10 and 1, respectively). Data correspond to net values of tetramer$^+$ cells after subtraction of staining with a negative control tetramer (HEL$_{14-22}$/IA^{g7}). See Supplementary Fig. 3 for additional details. **f**, The magnitude of CD4$^+$ Treg expansion in response to 10 injections of various preparations of BDC2.5mi/IA^{g7}-PF-M is dissociated from pMHC valency and density. Data correspond to net values of tetramer$^+$ cells after subtraction of staining with a negative control tetramer (HEL$_{14-22}$/IA^{g7}). Data correspond to 5, 2, 9, 6, 4, 5 and 4 mice per pMHC–NP batch (carrying 29, 36, 39, 45, 53, 59 and 61 pMHCs, respectively). **g**,**h**, Per cent increase in the mean fluorescence intensity of CD49b on BDC2.5mi/IA^{g7} tetramer$^+$ cells expanded *in vivo* by different BDC2.5mi/IA^{g7}-NP preparations as a function of pMHC density (**g**) ($n = 8$, 6, 2, 21, 4 and 5 mice, respectively) and dose (**h**) ($n = 8$, 16, 10 and 1 mice, respectively). P values in **e**–**h** were calculated by Pearson's correlation test. NS, statistically not significant.

© 2017 Macmillan Publishers Limited, part of Springer Nature. All rights reserved.

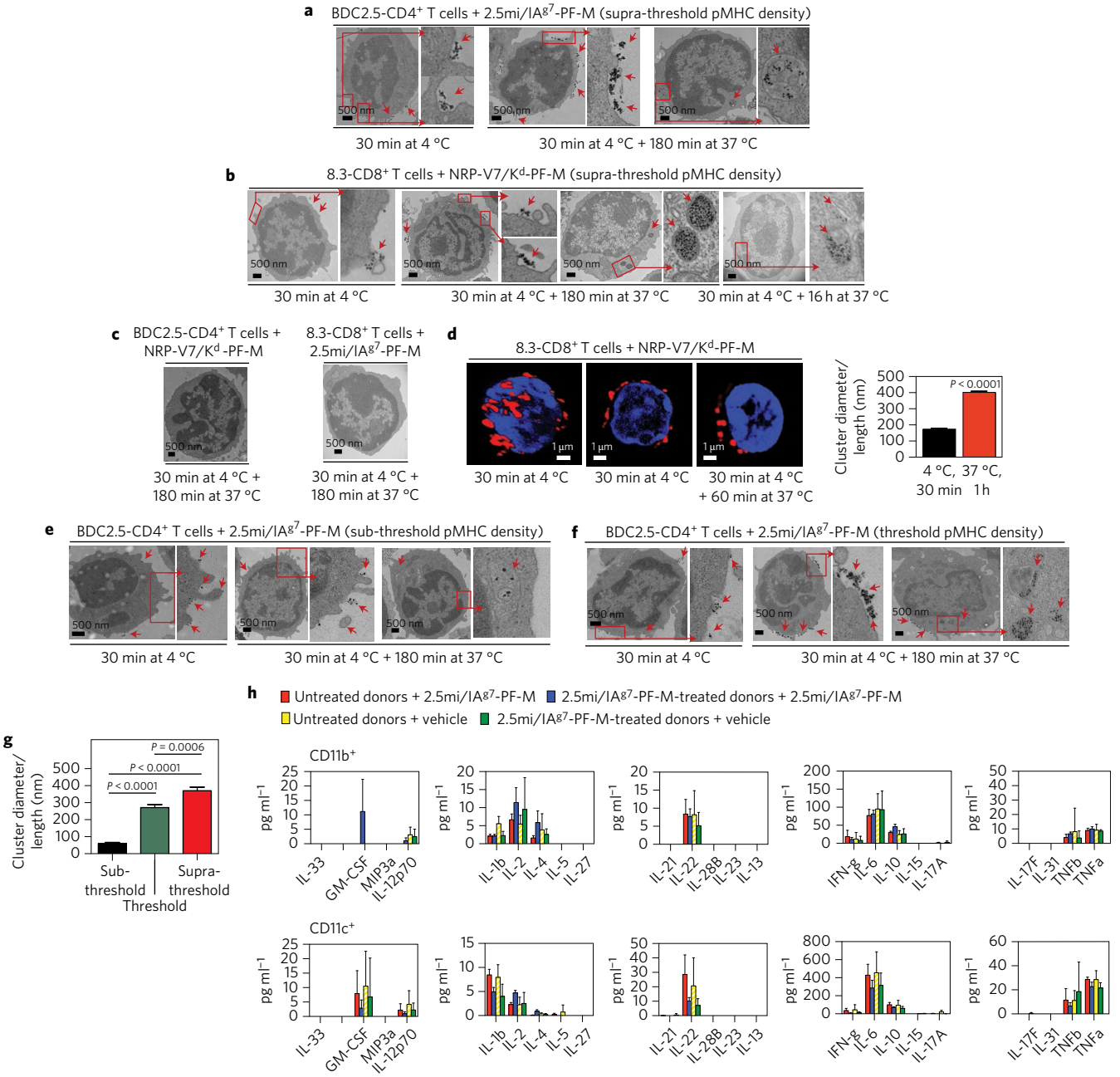

Figure 4 | Sustained binding and clustering of pMHC–NPs on cognate T cells as a function of pMHC density, and sterile internalization by macrophages or DCs. a,**b**, 2D TEM images of BDC2.5mi-CD4$^+$ (**a**) or 8.3-CD8$^+$ T cells (**b**) incubated with BDC2.5mi/IA^{g7}- or NRP-V7/K^d-PF-M, respectively, coated at supra-threshold pMHC densities (46 pMHCs per NP). The two right panels in **a** and the four right panels in **b** show the presence of NPs in intracellular vesicles after a 3 h incubation at 37 °C. **c**, 2D TEM images of BDC2.5mi-CD4$^+$ and 8.3-CD8$^+$ T cells incubated with non-cognate NRP-V7/K^d-PF-M and BDC2.5mi/IA^{g7}-PF-M, respectively. **d**, Left 3D image: super-resolution microscopy of 8.3-CD8$^+$ T cells incubated with NRP-V7/K^d-PF-M-Alexa-647 at 4 °C for 30 min. Middle and right 2D images: T cells incubated at 4 °C for 30 min and at 4 °C for 30 min followed by 37 °C for 1 h. The histogram plot shows that the NP clusters increase in diameter with incubation time and temperature (179.1 ± 4.6 nm to 401.7 ± 4.2 nm; $n = 100$ clusters per condition; P values were calculated by a Mann–Whitney U test). Red, NRP-V7/K^d-PF-M-Alexa-647; blue, DAPI. **e**,**f**, 2D TEM images of BDC2.5mi-CD4$^+$ T cells incubated with BDC2.5mi/IA^{g7}-PF-M preparations carrying sub-threshold (10 pMHCs per NP; **e**) or threshold (24 pMHCs per NP; **f**) pMHC densities. Four left panels in **e** and **f** show absence (**e**) or presence (**f**) of microclusters on the T-cell membrane. Two right panels in **e** and **f** show presence of intracellular vesicles. The red arrows in **a**,**b**,**e**,**f** show that they are NPs or clusters of NPs. **g**, Average size of microclusters in cells cultured in the presence of pMHC–NPs coated at sub-threshold (59.5 ± 6.5 nm) ($n = 59$ clusters on 9 cells), threshold (271.2 ± 17.3 nm) ($n = 57$ clusters on 12 cells) and supra-threshold valencies (370 ± 21.3 nm) ($n = 60$ clusters on 15 cells). P values were calculated by a Mann–Whitney U test. **h**, pMHC–PF-M do not trigger cytokine/chemokine secretion by splenic CD11b$^+$ or CD11c$^+$ cells. Data correspond to cells from four BDC2.5mi/IA^{g7}-PF-M-treated and four untreated mice, analysed in two independent experiments. None of the differences were statistically significant.

on TCR microcluster formation. We compared BDC2.5mi-IA^{g7}-NPs carrying pMHCs at sub-threshold, threshold and supra-threshold densities. Remarkably, NPs coated at sub-threshold densities bound to and were eventually internalized by cognate CD4$^+$ T cells but without forming clusters (Fig. 4e,g). In contrast, NPs coated at threshold densities readily triggered the formation of

© 2017 Macmillan Publishers Limited, part of Springer Nature. All rights reserved.

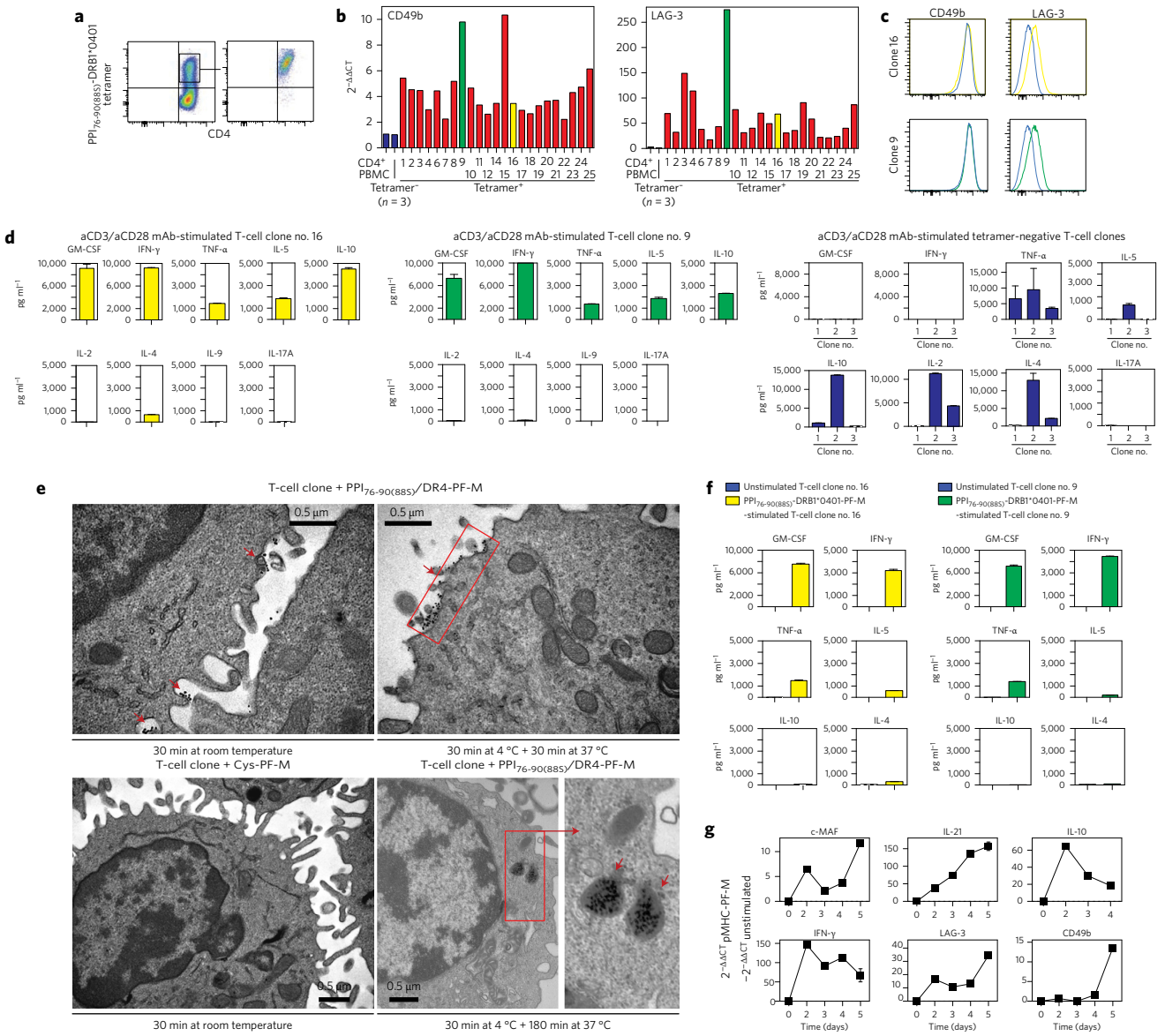

Figure 5 | Binding to, and agonistic properties of human autoimmune disease-relevant pMHC–NPs on human cognate TR1-like/poised CD4$^+$ T-cell clones. a, Left: pMHC tetramer flow cytometry profiles of human peripheral blood mononuclear cells (PBMCs) on successive culture with PPI$_{76-90(K88S)}$ peptide, plate-bound PPI$_{76-90(K88S)}$/DRB1*0401 pMHC monomers, and anti-CD28 plus IL-2. Right: T-cell clone generated from a PHA-P/rhIL-2 stimulated cell sorted from the tetramer$^+$ population on the left. **b**, Relative levels of CD49b and LAG-3 mRNA on 23 teramer$^+$ clones versus three tetramer$^-$ clones and bulk peripheral blood CD4$^+$ T cells. **c**, Flow cytometric analyses of CD49b and LAG-3 protein expression on tetramer$^+$ (double-positive) versus tetramer$^-$ clones (single CD49b$^+$). **d**, Secretion of various cytokines by two tetramer$^+$ clones (left and middle) and three tetramer$^-$ clones (right) in response to anti-CD3 and anti-CD28 mAb-coated beads. **e**, TEM of human TR1-like/poised cells incubated with PPI$_{76-90(K88S)}$/DRB1*0401-PF-Ms or control (Cys-conjugated) PF-Ms. Arrows point to representative nanoparticle clusters. **f**, Secretion of cytokines by clone no. 16 and clone no. 9 cells in response to cognate pMHC–NPs. **g**, Upregulation of TR1 cell-relevant transcripts by clone no. 16 in response to cognate pMHC–NPs versus baseline levels in unstimulated cells.

clusters, and the sizes of these clusters increased using NPs coated at supra-threshold densities (Fig. 4a,f,g). Therefore, pMHC density controls Treg cell conversion by promoting the sustained assembly of TCR microclusters, leading to rapid, robust and prolonged TCR signalling (Supplementary Fig. 2b).

The inability of peptide-coated NPs or microparticles (without the MHC component) to trigger TR1 cell formation in various autoimmune disease models[2], coupled to the inability of clodronate liposome treatment (which largely deletes macrophages but also dendritic cells (DCs)[17]) to suppress pMHC class II-NP-induced TR1 cell formation (Supplementary Fig. 4c), indicates that this process is antigen-presenting cell (APC)-independent. This, however, does not exclude a role for APCs in the uptake and degradation of these compounds. SEM of peritoneal macrophages and bone marrow-derived DCs revealed the presence of isolated (non-clustered) pMHC–NPs on the surface of macrophages and DCs (Supplementary Fig. 4d–f). Remarkably, TEM imaging demonstrated that macrophages and, to a lesser extent, DCs rapidly internalized both pMHC-coated and uncoated NPs, even at 4 °C, into endocytic vesicles (Supplementary Fig. 4g). Thus, unlike T cells, phagocytes rapidly phagocytose pMHC–NPs in a pMHC-independent manner without membrane retention or cluster formation. Importantly, *ex vivo* pMHC–NP challenge experiments using splenic CD11b$^+$ and CD11c$^+$ cells from pMHC–NP-treated and untreated NOD mice further indicated that pMHC–NP binding is a 'sterile' event that does not trigger cytokine/chemokine release (Fig. 4h).

© 2017 Macmillan Publishers Limited, part of Springer Nature. All rights reserved.

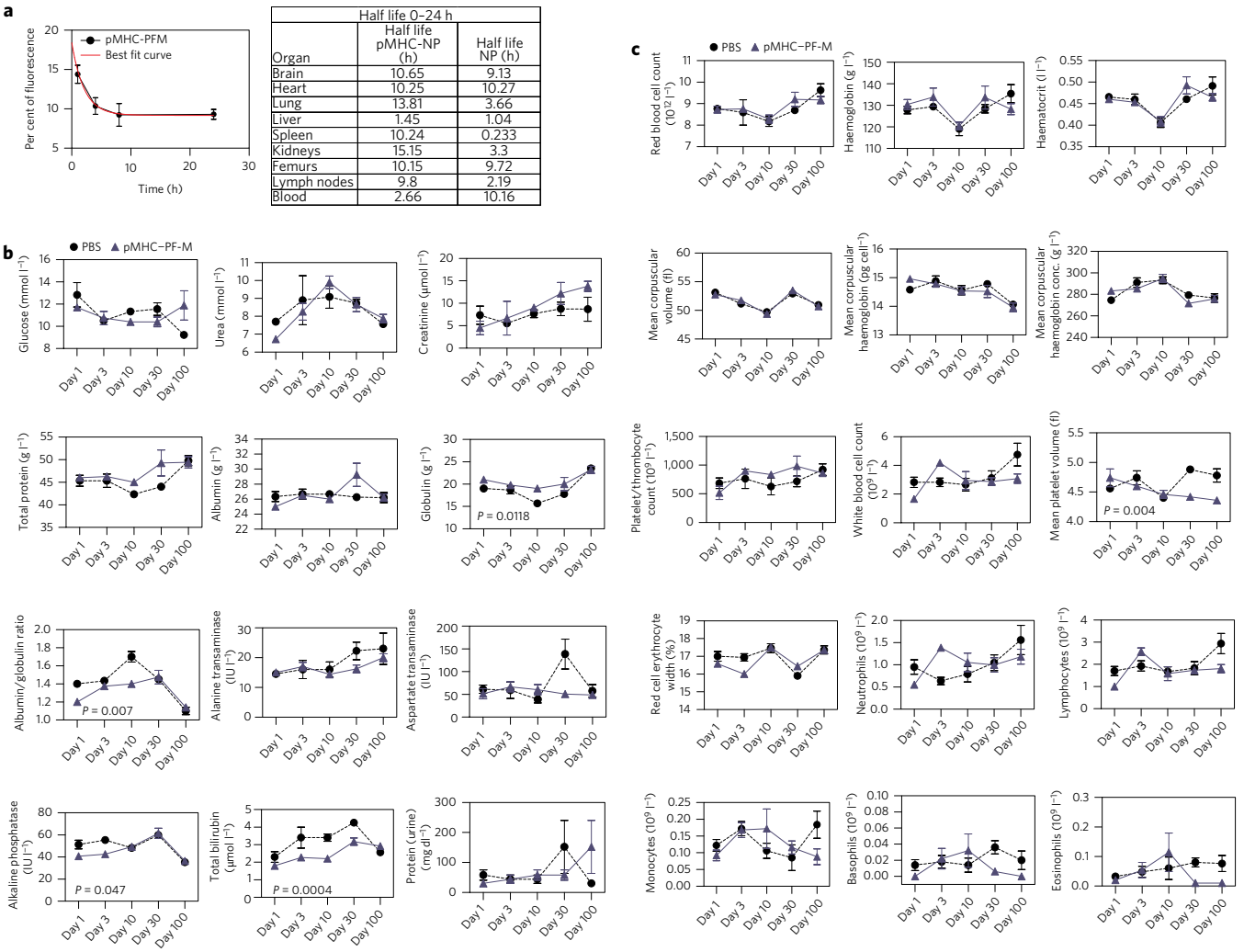

Half life 0–24 h		
Organ	Half life pMHC-NP (h)	Half life NP (h)
Brain	10.65	9.13
Heart	10.25	10.27
Lung	13.81	3.66
Liver	1.45	1.04
Spleen	10.24	0.233
Kidneys	15.15	3.3
Femurs	10.15	9.72
Lymph nodes	9.8	2.19
Blood	2.66	10.16

Figure 6 | Pharmacokinetics and toxicology of pMHC class II–PF-Ms in NOD mice. a, Representative tissue-specific (liver) fluorescence decay curves for pMHC conjugated and unconjugated PF-M, and derivation of the corresponding tissue-specific half-life times ($n = 3$ mice per treatment type and time point). **b**, Biochemical read-outs in plasma and total levels of protein in urine (last panel) ($n = 5$ mice per treatment type and time point). Cohorts of NOD mice ($n = 5$ mice per treatment type and time point) were injected with one dose of pMHC-conjugated NP (200 μg Fe) or PBS, and blood samples were collected at different time points. **c**, Haematological read-outs from the same samples collected for **b**. *P* values in **b**,**c** were calculated via two-way ANOVA. Only *P* values < 0.05 are shown. All other read-outs were statistically not significant.

To investigate if human TR1-poised CD4$^+$ T cells bind and respond to pMHC class II-PF-NPs like their murine conterparts, we generated human TR1-poised CD4$^+$ T-cell clones specific for the preproinsulin (PPI)$_{76–90(K88S)}$/DRB1*0401 pMHC by passaging peptide-challenged peripheral blood CD4$^+$ T cells of a T1D patient on pMHC-coated plates. Single pMHC-tetramer-positive and -negative cells were then sorted and expanded by stimulation with phytohemagglutinin-P and rhIL-2 (Fig. 5a). Quantitative reverse transcription-polymerase chain reaction (RT-PCR) revealed that 23/23 tetramer$^+$ clones expressed several fold higher levels of CD49b and especially LAG-3, than their three tetramer$^-$ counterparts or peripheral blood CD4$^+$ T cells (Fig. 5b). Additional flow cytometry studies with two tetramer$^+$ clones and the three tetramer$^-$ clones revealed that the former co-expressed both CD49b and LAG-3 on the cell surface (Fig. 5c), consistent with a TR1-poised phenotype[18,19]. In addition, anti-CD3/anti-CD28 mAb challenge triggered the secretion of high levels of the TR1 cytokines granulocyte-macrophage colony-stimulating factor (GM-CSF), IFNγ, IL-10, TNFα and IL-5 (refs 18,19), but not cytokines expressed by Th1, Th2, Th9 or Th17 cells (IL-2, IL-4, IL-9 or IL-17) (Fig. 5d, left). None of the three tetramer$^-$ clones displayed this phenotype (Fig. 5d, right).

TEM of cells cultured in the presence of PPI$_{76–90(K88S)}$/DRB1*0401-PF-NPs revealed a pMHC–NP-binding geometry and kinetics similar to those observed for mouse CD4$^+$ T cells (Fig. 5e). This was associated with secretion of GM-CSF, IFNγ and TNFα, albeit not IL-5 or IL-10 (Fig. 5f), consistent with the costimulation-dependent secretion of IL-10 in mouse TR1-like CD4$^+$ T cells[2]. Further pMHC–NP exposure resulted in the upregulation of the TR1 cell transcrips c-MAF, IL-21, IL-10, IFNγ, CD49b and LAG-3 (Fig. 5g).

Collectively, these data indicate that human autoimmune disease-relevant pMHC–NPs bind to cognate human patient-derived TR1-poised CD4$^+$ T cells as clusters that remain on the plasma membrane for a sustained period of time and trigger the upregulation of TR1 cell transcripts without triggering IL-10 secretion. Together with the ability of human T1D-relevant pMHC class II–NPs to trigger the formation and expansion of human TR1-like CD4$^+$ T cells in humanized mice[2], these new data provide further compelling evidence supporting the translational significance of these compounds.

Biodistribution, pharmacokinetics and toxicology of PF-NPs

Exposure of NRP-V7/K^d-PF-NPs with mouse serum at 37 °C *in vitro* resulted in a rapid loss of activity (~40%) during the first

© 2017 Macmillan Publishers Limited, part of Springer Nature. All rights reserved.

hour, followed by a much slower decline afterwards (~5% h^{-1}) (Supplementary Fig. 5a), suggesting that the pMHC coat is subject to proteolytic degradation or masking by plasma components. Comparison of the rates of accumulation and clearance of fluorochrome-labelled pMHC, PF-NPs and pMHC–PF-NPs *in vivo* indicated that they are distributed systemically (Fig. 6a and Supplementary Fig. 5b–d). However, whereas pMHC delivered either as monomers or as PF-NP conjugates are consistently enriched in the kidney, PF-NPs are preferentially enriched in the liver and gut (Supplementary Fig. 5d). This suggests that the NP component can be excreted via the hepatobiliary system[20–22]. The fluorescence signal observed in the kidney and urine likely corresponds to free fluorochome (Cyto670) or to proteolytic fragments of pMHC released from the pMHC coat by serum proteases, as suggested by the data in Supplementary Fig. 5a. Fluorescence intensity decay in different organs followed one-phase exponential kinetics (Fig. 6a) and were consistent with very short half-lives for the pMHC and the NP components of pMHC–PF-NPs (especially in the liver and blood for the pMHC, and in phagocyte-rich organs such as the liver, lungs, kidneys and lymph nodes for the NPs) (Fig. 6a).

To investigate possible off-target effects, we performed a zebrafish embryo development screen using PF-M and pMHC–PF-M. No mortality or morphological (17 endpoints) or touch response abnormalities were seen over a broad range of concentrations (Supplementary Fig. 6). Furthermore, intravenous delivery of pMHC–PF-M did not increase the serum concentrations of a broad range of cytokines and chemokines versus sham-treated controls (human injectable saline) within 8 h after injection, indicating that they do not induce a 'cytokine storm' (Supplementary Fig. 7a). pMHC–PF-NPs also failed to induce significant changes in a broad range of serum biochemical and haematological parameters or abnormalities in the urine versus PBS-treated mice (Fig. 6b,c and Supplementary Table 4).

Multi-organ histopathology did not reveal significant abnormalities, as compared to PBS (Supplementary Table 5). Likewise, ultrastructural studies of the kidneys of mice treated with pMHC–PF-M or ferumoxytol (a FDA-approved iron oxide NP, IONP) versus PBS demonstrated the lack of NP accumulation in the glomeruli or structural abnormalities (Supplementary Fig. 7b).

Conclusion

We have described a novel and simple manufacturing process that consistently yields highly stable and potent iron oxide-based Treg-triggering/expanding nanomedicines. These pMHC–PF-NP preparations are biocompatible, devoid of off-target effects, and have no appreciable systemic or organ-specific toxicity. Whereas the NP component of these compounds functions as a ligand multimerization platform that is essential for biological activity, the directionally positioned ligands provide cell-targeting specificity.

It has been established that the biodistribution profile, blood residence time, proclivity for organ accumulation, biodegradability, bystander immune-stimulatory activity and toxic potential of NP-based compounds are a function of several parameters, including the chemical nature of the NP core[23]. Iron oxide NPs offer key advantages over other inorganic or organic NP types. They are rapidly taken up by phagocytes[24,25], are biodegradable, recycled into normal iron metabolism pathways and thus do not accumulate in tissues[20]. The PF-NP design aimed not only to simplify the manufacturing of a high-capacity NP in a novel single-step reaction, but also to maximize the pharmacodynamic properties of pMHC–NPs without compromising safety. The circulating half-life of IONPs decreases with NP size, and pegylation increases their plasma half-life[26]. The size and circulating half-life of our pegylated PF-M design (44 nm hydrodynamic diameter, ~10 h) fall between the values of clinically approved dextran-coated IONPs such as Ferumoxide and Ferumoxtran-10 (80–150 nm versus 20–40 nm, respectively), which have circulating half-lives of <0.5 h to ~30 h, respectively[27,28]. Another safety concern relates to the ability of NP-based compounds to activate phagocytes, leading to non-specific cytokine secretion. This has been documented for gold colloids, dendrimers, polymers and lipid nanoparticles among others[29–34]. pMHC–PF-NPs do not promote cytokine/chemokine secretion by $CD11b^+$ or $CD11c^+$ cells, do not impair these cells' responsiveness to innate immune stimuli such as lipopolysaccharides, and do not trigger a cytokine storm *in vivo*.

Using these compounds, we have defined the fundamental principles guiding the optimal design of pMHC–NP formulations aimed at expanding autoantigen-specific regulatory T cells *in vivo*. The optimal pMHC–NP design consists of small particles coated with pMHC monomers at high densities. Whereas pMHC density is responsible for the Treg-triggering potency of these compounds, total pMHC dose is associated with their Treg-expanding properties. The binding geometry of these compounds to cognate T cells accounts for the observed pMHC-density effects. Closely apposed pMHC monomers on the NP surface would facilitate the repeated re-engagement of transiently dissociated pMHC monomers on individual NPs, thus delaying TCR internalization and lengthening the half-life values ($t_{1/2}$s) of individual TCR–pMHC interactions[13,35]. The cytoskeletal rearrangemetns triggered by the resulting signalling events would then promote the sustained assembly of proximal pMHC–NP–TCR units into large TCR microclusters[36], further amplifying the duration and magnitude of TCR signalling[14]. High pMHC densities would also facilitate the cooperative propagation of conformational changes and associated downstream signalling events from pMHC-bound TCRs to their unbound neighbours[37,38], both within and between individual NPs on membrane clusters[39]. This interpretation, based on both experimental data and *in silico* mathematical and biophysical modelling, is compatible with both the kinetic proofreading[40] and serial TCR engagement models[41] of T-cell activation. The discovery that pMHC density is responsible for the remarkable and unanticipated immunotherapeutic effect caused by the supra-physiological receptor triggering properties of these compounds defines a critical design principle for ligand-based NP compounds that is likely to be applicable to other areas of biology.

Methods

Methods and any associated references are available in the online version of the paper.

Received 9 June 2016; accepted 6 March 2017;
published online 24 April 2017

References

1. Tsai, S. *et al.* Reversal of autoimmunity by boosting memory-like autoregulatory T cells. *Immunity* **32,** 568–580 (2010).
2. Clemente-Casares, X. *et al.* Expanding antigen-specific regulatory networks to treat autoimmunity. *Nature* **530,** 434–440 (2016).
3. Clemente-Casares, X., Tsai, S., Yang, Y. & Santamaria, P. Peptide-MHC-based nanovaccines for the treatment of autoimmunity: a "one size fits all" approach? *J. Mol. Med.* **89,** 733–742 (2011).
4. McLarnon, A. IBD: regulatory T-cell therapy is a safe and well-tolerated potential approach for treating refractory Crohn's disease. *Nat. Rev. Gastroenterol. Hepatol.* **9,** 509–516 (2012).
5. Desreumaux, P. *et al.* Safety and efficacy of antigen-specific regulatory T-cell therapy for patients with refractory Crohn's disease. *Gastroenterology* **143,** 1207–1217 (2012).
6. Xie, J. *et al.* One-pot synthesis of monodisperse iron oxide nanoparticles for potential biomedical applications. *Pure Appl. Chem.* **78,** 1003–1014 (2006).
7. Rojo, J. M. & Portoles, P. A symmetrical view of the T-cell receptor-CD3 complex. *Immunol. Today* **12,** 377–378 (1991).
8. Fernandez-Miguel, G. *et al.* Multivalent structure of an αβT cell receptor. *Proc. Natl Acad. Sci. USA* **96,** 1547–1552 (1996).
9. Arechaga, I. *et al.* Structural characterization of the TCR complex by electron microscopy. *Int. Immunol.* **22,** 897–903 (2010).

© 2017 Macmillan Publishers Limited, part of Springer Nature. All rights reserved.

10. Scholten, K. B. *et al.* Preservation and redirection of HPV16E7-specific T cell receptors for immunotherapy of cervical cancer. *Clin. Immunol.* **114,** 119–129 (2005).
11. Schamel, W. W. & Alarcon, B. Organization of the resting TCR in nanoscale oligomers. *Immunol. Rev.* **251,** 13–20 (2013).
12. Lillemeier, B. F. *et al.* TCR and Lat are expressed on separate protein islands on T cell membranes and concatenate during activation. *Nat. Immunol.* **11,** 90–96 (2010).
13. Zhong, L. *et al.* NSOM/QD-based direct visualization of CD3-induced and CD28-enhanced nanospatial coclustering of TCR and coreceptor in nanodomains in T cell activation. *PLoS ONE* **4,** e5945 (2009).
14. Yokosuka, T. *et al.* Newly generated T cell receptor microclusters initiate and sustain T cell activation by recruitment of Zap70 and SLP-76. *Nat. Immunol.* **6,** 1253–1262 (2005).
15. Choudhuri, K. & Dustin, M. L. Signaling microdomains in T cells. *FEBS Lett.* **584,** 4823–4831 (2010).
16. Sherman, E. *et al.* Functional nanoscale organization of signaling molecules downstream of the T cell antigen receptor. *Immunity* **35,** 705–720 (2011).
17. Weisser, S. B., van Rooijen, N. & Sly, L. M. Depletion and reconstitution of macrophages in mice. *J. Vis. Exp.* **66,** e4105 (2012).
18. Gagliani, N. *et al.* Coexpression of CD49b and LAG-3 identifies human and mouse T regulatory type 1 cells. *Nat. Med.* **19,** 739–746 (2013).
19. Roncarolo, M. G., Gregori, S., Bacchetta, R. & Battaglia, M. Tr1 cells and the counter-regulation of immunity: natural mechanisms and therapeutic applications. *Curr. Top Microbiol. Immunol.* **380,** 39–68 (2014).
20. Gu, L., Fang, R. H., Sailor, M. J. & Park, J. H. *In vivo* clearance and toxicity of monodisperse iron oxide nanocrystals. *ACS Nano* **6,** 4947–4954 (2012).
21. Kolosnjaj-Tabi, J. *et al.* The one year fate of iron oxide coated gold nanoparticles in mice. *ACS Nano* **9,** 7925–7939 (2015).
22. Chou, L. Y., Zagorovsky, K. & Chan, W. C. DNA assembly of nanoparticle superstructures for controlled biological delivery and elimination. *Nat. Nanotech.* **9,** 148–155 (2014).
23. Alexis, F., Pridgen, E., Molnar, L. K. & Farokhzad, O. C. Factors affecting the clearance and biodistribution of polymeric nanoparticles. *Mol. Pharm.* **5,** 505–515 (2008).
24. Borchard, G. & Kreuter, J. The role of serum complement on the organ distribution of intravenously administered poly (methyl methacrylate) nanoparticles: effects of pre-coating with plasma and with serum complement. *Pharm. Res.* **13,** 1055–1058 (1996).
25. Armstrong, T. I., Davies, M. C. & Illum, L. Human serum albumin as a probe for protein adsorption to nanoparticles: relevance to biodistribution. *J. Drug Target* **4,** 389–398 (1997).
26. Roohi, F., Lohrke, J., Ide, A., Schutz, G. & Dassler, K. Studying the effect of particle size and coating type on the blood kinetics of superparamagnetic iron oxide nanoparticles. *Int. J. Nanomed.* **7,** 4447–4458 (2012).
27. Bourrinet, P. *et al.* Preclinical safety and pharmacokinetic profile of ferumoxtran-10, an ultrasmall superparamagnetic iron oxide magnetic resonance contrast agent. *Invest. Radiol.* **41,** 313–324 (2006).
28. Varallyay, P. *et al.* Comparison of two superparamagnetic viral-sized iron oxide particles ferumoxides and ferumoxtran-10 with a gadolinium chelate in imaging intracranial tumors. *AJNR Am. J. Neuroradiol.* **23,** 510–519 (2002).
29. Scholer, N. *et al.* Effect of solid lipid nanoparticles (SLN) on cytokine production and the viability of murine peritoneal macrophages. *J. Microencapsul.* **17,** 639–650 (2000).
30. Scholer, N., Hahn, H., Muller, R. H. & Liesenfeld, O. Effect of lipid matrix and size of solid lipid nanoparticles (SLN) on the viability and cytokine production of macrophages. *Int. J. Pharm.* **231,** 167–176 (2002).
31. Fifis, T. *et al.* Size-dependent immunogenicity: therapeutic and protective properties of nano-vaccines against tumors. *J. Immunol.* **173,** 3148–3154 (2004).
32. Shvedova, A. A. *et al.* Unusual inflammatory and fibrogenic pulmonary responses to single-walled carbon nanotubes in mice. *Am. J. Physiol. Lung Cell Mol. Physiol.* **2005,** L698–L708 (2005).
33. Vallhov, H. *et al.* The importance of an endotoxin-free environment during the production of nanoparticles used in medical applications. *Nano Lett.* **6,** 1682–1686 (2006).
34. Mottram, P. L. *et al.* Type 1 and 2 immunity following vaccination is influenced by nanoparticle size: formulation of a model vaccine for respiratory syncytial virus. *Mol. Pharm.* **4,** 73–84 (2007).
35. Huppa, J. B. *et al.* TCR-peptide-MHC interactions *in situ* show accelerated kinetics and increased affinity. *Nature* **463,** 963–967 (2010).
36. Bunnell, S. C. *et al.* T cell receptor ligation induces the formation of dynamically regulated signaling assemblies. *J. Cell Biol.* **158,** 1263–1275 (2002).
37. Gil, D., Schamel, W. W., Montoya, M., Sanchez-Madrid, F. & Alarcon, B. Recruitment of Nck by CD3ϵ reveals a ligand-induced conformational change essential for T cell receptor signaling and synapse formation. *Cell* **109,** 901–912 (2002).
38. Minguet, S., Swamy, M., Alarcon, B., Luescher, I. F. & Schamel, W. W. Full activation of the T cell receptor requires both clustering and conformational changes at CD3. *Immunity* **26,** 43–54 (2007).
39. Martinez-Martin, N. *et al.* Cooperativity between T cell receptor complexes revealed by conformational mutants of CD3ϵ. *Sci. Signal.* **2,** ra43 (2009).
40. McKeithan, T. W. Kinetic proofreading in T-cell receptor signal transduction. *Proc. Natl Acad. Sci. USA* **92,** 5042–5046 (1995).
41. Valitutti, S., Muller, S., Cella, M., Padovan, E. & Lanzavecchia, A. Serial triggering of many T-cell receptors by a few peptide–MHC complexes. *Nature* **375,** 148–151 (1995).

Acknowledgements

We thank S. Thiessen, J. Erickson and J. Luces for technical assistance, and L. Kennedy for flow cytometry. We acknowledge T. DiLorenzo for providing JurMA cells, H. Benediktsson for structural analyses of kidney TEM, R. Interior for amino acid analysis, W. White and D. Cramb for assistance with GD-mass spectrometry, FTIR and DLS, T. Furstenhaupt and W. Dong for SEBD and TEM, J.M. Rebled, A. Garcia, R. Rivera and A. Martínez from the TEM–SEM unit from the University of Barcelona (CCiT-UB) for TEM analyses of human T-cell clone:pMHC–NP conjugates, and the CMHD Unit at the Lunenfeld–Tanenbaum Institute for haematology and biochemistry. This work was funded by the Collaborative Health Research Program of the Canadian Institutes of Health Research (CIHR) and the Natural Sciences and Engineering Research Council of Canada, the Instituto de Investigaciones Sanitarias Carlos III, the Ministerio de Economia y Competitividad of Spain (MINECO), and the Sardà Farriol Research Programme. X.C.C. was supported by studentships from the AXA Research Fund and the endMS network. K.S. is funded by Eyes' High/Alberta Innovates-Technology Futures, Alberta Innovates–Health Solutions (AI-HS) and Banting-CIHR fellowships. C.S.U. is supported by AI-HS and Banting-CIHR fellowhips. R.H.N. is supported by studentships from AI-HS and CIHR. S.W.L. was partially supported by a studentship from Fonds de Recherche du Quebec - Nature et Technologies. J.B. was supported by a Rio Hortega fellowship from the Ministry of Economy and Competitiveness of Spain and by a fellowship from the European Association for the Study of Diabetes (EASD). P.Serra is a Ramon y Cajal investigator supported by a Juvenile Diabetes Research Foundation Career Development Award. P.Santamaria is Scientist of the Alberta Innovates-Health Solutions and a scholar of the IISCIII. The JMDRC is supported by the Canadian Diabetes Association (CDA).

Author contributions

S.S. and Y.Y. developed and produced all the pMHC–NPs, and data for Figs 1, 2a–j, 4a–c, 4e–g and Supplementary Figs 1, 4d–f,g, 5a and 7b, in collaboration with K.S.; K.S. produced data for Figs 2l, 4d, and Supplementary Figs 4a–c and 8. X.C. produced data for Figs 3e–h and 4i and Supplementary Figs 3 and 7a, in collaboration with J.Y.; P. Solé produced the JurMA TCR/mCDA transfectants and produced the data for Fig. 2k. J.Y. produced the data for Supplementary Fig. 4c. C.S.U. and R.H.N. produced murine pMHCs for this study. C.F. purified human pMHCs. J.B., A.C. and P. Serra produced data for Fig. 5. Q.D., F.S. and W.C.W.C. produced data for Fig. 6 and Supplementary Fig. 5. S.W.L. and A.K. generated all the mathematical models and produced Fig. 3a–d and Supplementary Figs 9 and 10. P.D. and M.A. contributed expertise in confocal microscopy and SEM. R.T. generated the zebrafish embryo toxicology data for Supplementary Fig. 6. S.N. carried out the multi-organ histopathology. P. Santamaria designed and supervised the study and wrote the manuscript with the assistance of S.S.

Additional information

Supplementary information is available in the online version of the paper. Reprints and permissions information is available online at www.nature.com/reprints. Publisher's note: Springer Nature remains neutral with regard to jurisdictional claims in published maps and institutional affiliations. Correspondence and requests for materials should be addressed to Y.Y. and P.S.

Competing financial interests

P. Santamaria is scientific founder of Parvus Therapeutics Inc. and has a financial interest in the company.

© 2017 Macmillan Publishers Limited, part of Springer Nature. All rights reserved.

Methods

Mice. NOD/Lt mice were from the Jackson Lab (Bar Harbor, ME). 17.4α/8.3β (8.3-NOD) and BDC2.5-NOD mice (expressing transgenic T-cell receptors for $IGRP_{206-214}$ or NRP-V7/K^d and 2.5 mi/IA^{g7}, respectively) have been described[42–44]. The experiments described herein were not blinded and were approved by the University of Calgary Animal Care Committee and by the Faculty of Medicine and Pharmacy Animal Care Committee at the University of Toronto. No samples of animals were excluded from the analyses reported.

pMHC production. Recombinant pMHC class I were produced by re-folding MHC class I heavy and light chains expressed in bacteria in the presence of peptide, followed by purification via gel filtration and anion exchange chromatography[45,46], or by expressing glycine-serine (GS) linker-tethered single-chain MHC class I complexes in mycoplasma-free lentiviral-transduced freestyle chinese hamster ovary (CHO) cells[47]. Recombinant pMHC class II were produced in CHO cells transduced with lentiviruses encoding a monocistronic message in which the peptide-MHCβ and MHCα chains were separated by a ribosome skipping P2A-coding sequence[48]. The secreted proteins were purified using strep-tag and/or nickel columns and used for NP coating or biotinylated to produce pMHC tetramers using fluorochrome-conjugated streptavidin (Supplementary Figs 1b and 5a).

pMHC tetramer staining. Phycoerythrin (PE)-conjugated TUM/K^d, NRP-V7/K^d, $IGRP_{206-214}$/K^d, HEL_{14-22}/IA^{g7} and BDC2.5mi/IA^{g7} tetramers were prepared using biotinylated pMHC monomers and used to stain peripheral T cells as described[49,50].

NP synthesis. Gold nanoparticles (GNPs) were synthesized by chemical reduction of chloroauric acid ($HAuCl_4$) with sodium citrate as described[51]. The SFP series iron oxide (Fe_3O_4) NPs were produced by thermal decomposition of iron acetylacetonate in organic solvents in the presence of surfactants, then rendered solvent in aqueous buffers by pegylation[6,52,53] using different dopamine-conjugated PEGs (DPA-PEG, 3.5 kDa) (Supplementary Table 1; Jenkem Tech). The monodisperse SFP NPs were stored in water. The concentration of iron was determined spectrophotometrically at 410 nm in 2 N hydrochloric acid (HCl). Based on the structure and diameter of SFP NPs[6,52], SFP solutions containing 1 mg of iron contain 5×10^{14} NPs.

We subsequently developed a new iron oxide NP design to produce, also by thermal decomposition but in a single step, pegylated iron oxide NPs in the absence of surfactants (PF series). PEG molecules were used as an *in situ* surface-coating agent. In a typical reaction, 3 g PEG (2 kDa) was melted in a 50 ml round bottom flask at 100 °C and then mixed with 7 ml of benzyl ether and 2 mmol $Fe(acac)_3$. The reaction was stirred for 1 h and heated to 260 °C with reflux for 2 h. The mixture was cooled to room temperature and mixed with 30 ml water. Insoluble materials were removed by centrifugation at 2,000*g* for 30 min. We were able to generate iron oxide NPs with most, albeit not all of the PEG molecules tested (Supplementary Table 1). The size of the iron oxide NPs varied depending on the functional groups (Supplementary Tables 1 and 2). The NPs could be readily purified using magnetic (MACS) columns (Miltenyi Biotec) or an IMag cell separation system (BD BioSciences). The purified iron oxide NPs were stored in water at room temperature or 4 °C without any detectable aggregation. NP concentration was calculated as described above.

pMHC conjugation to NPs. pMHC conjugation to NPs produced with PEG linkers carrying distal primary amine (–NH_2) or carboxyl (–COOH) groups was achieved via the formation of amide bonds in the presence of 1-ethyl-3-[3-dimethylaminopropyl]carbodiimide hydrochloride (EDC). To conjugate pMHC to maleimide-functionalized NPs (SFP-M and PF-M; Supplementary Table 2), pMHC molecules engineered to encode a free C-terminal Cys were mixed with NPs in 40 mM phosphate buffer, pH 6.0, containing 2 mM ethylenediaminetetraacetic acid (EDTA), 150 mM NaCl, and incubated overnight at room temperature. Click chemistry was used to conjugate pMHC to NPs functionalized with azide groups (SFP-Z; Supplementary Table 2 and Supplementary Fig. 2a). pMHCs were incubated with dibenzocyclooctyne-*N*-hydroxysuccinimidyl ester (DBCO-NHS, Click Chemistry Tools) for 2 h at room temperature. Free DBCO molecules were removed by dialysis. pMHC–DBCO conjugates were incubated with SFP-Z for 2 h. Unconjugated pMHCs in the different reactions were removed by dialysis against PBS, pH 7.4, at 4 °C through 300 kDa cut-off membranes (Spectrum Labs). Alternatively, pMHC-conjugated NPs were purified by magnetic separation. The conjugated NPs were concentrated by ultrafiltration through Amicon Ultra-15 (100 kDa cut-off) and stored in PBS.

NP characterization. The size and dispersity of unconjugated and pMHC-conjugated NPs were assessed via TEM (Hitachi H7650) and DLS (Zetasizer, Malvern). The chemical nature of the iron oxide core of the PF series of NPs was evaluated using SEBD. The surface properties were evaluated with FTIR using a Nicolet FTIR spectrophotometer on an attenuated total reflection mode. Pegylated and pMHC–NPs were also analysed via 0.8% agarose gel electrophoresis, native- and denaturing 10% SDS-PAGE.

pMHC valency measurements. To quantify pMHC valency, we measured the pMHC concentration of the pMHC–NP preparations using different approaches, including Bradford assay (Thermo Scientific), amino acid analysis (high-performance liquid chromatography (HPLC)-based quantification of 17 different amino acids in hydrolysed pMHC–NP) (University of Toronto) and dot-enzyme-linked immunosorbent assay (dot-ELISA), and the values converted to ratios of pMHC molecular number to NP number. Briefly, in the dot-ELISA approach, pMHC-conjugated and unconjugated NPs and pMHC monomer solutions (as standards) were serially diluted in PBS and adsorbed to a polyvinylidene fluoride membrane in a multiwell filter plate. The plate was incubated with pMHC-specific primary antibodies (Abs) (that is, anti-β2M and anti-K^d for pMHC class I–NPs, clones 2M2 and SF1-1.1, respectively; BioLegend), followed by horseradish peroxidase (HRP)- or alkaline phosphatase (AP)-conjugated secondary Abs. On development of the colour reactions, the absorbance of the supernatants was measured at 450 nm. Because the values generated by these different methods were similar (Supplementary Fig. 8), the Bradford assay (using unconjugated NPs as blanks) became the method of choice.

Endotoxin-free pMHC–NP production and endotoxin measurements. All glassware were baked in a drying oven at 200 °C for 2 h. All high-speed centrifuge tubes, rubber stoppers, containers and stir bars were pre-treated with 2 M NaOH overnight, and rinsed with endotoxin-free water prior to being used. Buffers were prepared in endotoxin-free water (Cellgro, Fisher Scientific). Processing, conjugation and purification of NPs were carried out in a laminar flow hood. And gloves were sprayed with 70% ethanol. The levels of endotoxin in pMHC, NPs and pMHC–NPs were monitored using a chromogenic LAL endotoxin assay kit (Genscript)[54,55]. These steps effectively reduced levels of endotoxin in pMHC–NPs to <0.01 EU ml^{-1} (assay detection limit; EU, endotoxin units).

TCR signalling in TCR/mCDA-transfected JurMA cells. The TCRα and TCRβ cDNAs encoding the BDC2.5-TCR were generated from BDC2.5-$CD4^+$ T-cell-derived mRNA using the 5' RACE System for Rapid Amplification of cDNA Ends, version 2.0 kit (Thermo Fisher Scientific), and subcloned as a P2A-tethered single open-reading frame into a retroviral vector upstream of an IRES-eGFP cassette. The human $CD3^+$/TCRβ–JurMA reporter cell line (expressing NFAT-driven luciferase) was transduced with retroviruses encoding murine CD4 and BDC2.5-TCRαβ. eGFP and mCD4 double-positive cells were sorted by flow cytometry and stained with PE-labelled BDC2.5/IA^{g7} pMHC tetramers to confirm specificity.

To measure NFAT-driven expression of luciferase, wild-type and BDC2.5/$mCD4^+$ JurMA cells were plated at 500,000 cells per well in 200 μl of Dulbecco's modified eagle's medium (DMEM) (Sigma-Aldrich) supplemented with 10% foetal bovine serum (FBS) (Sigma-Aldrich) in the presence or absence of 20 ng ml^{-1} PMA plus 0.5 μM Ionomycin (Sigma-Aldrich), 10 μg ml^{-1} of anti-hCD3ε mAb (OKT3, BD Biosciences) or 12.5 μg ml^{-1} of BDC2.5/IA^{g7}-coated PF-M. Cells were washed three times with PBS and 10^5 cells lysed in 20 μl cell culture lysis reagent (Promega) and incubated with 100 μl of luciferase assay reagent (Promega) in opaque white plates (Greiner Bio One International GmbH) using a Veritas Microplate Luminometer (Promega) with injectors. Luciferase activity was expressed as relative luminescence units (RLUs), normalized to the luciferase activity of non-stimulated cells.

pMHC–NP therapy of NOD mice. Cohorts of 10-week-old female NOD mice were injected intravenously with pMHC-coated NPs in PBS twice a week for 5 weeks. Increases in the size of $tetramer^+$ $CD8^+$ or $CD4^+$ T-cell pools in blood, spleen, lymph nodes and/or marrow, as well as their phenotypic properties, were assessed by flow cytometry as described[1,2].

Clodronate liposome treatment. NOD.Ltj mice were injected intraperitoneally with PBS or clodronate liposomes (0.01 ml per g body-weight, following the manufacturer's instructions; www.ClodronateLiposome.com) on days –4 and –1 relative to the initiation of BDC2.5mi/IA^{g7}-PFM treatment (7.5 μg pMHC per dose). The mice were treated twice a week for 5 weeks with both clodronate liposomes or PBS and pMHC–NPs. To measure the efficiency of phagocyte-depletion, haemolysed and collagenase D-treated spleens were stained with CD11c- and F4/80-specific mAbs. As described previously, clodronate liposome treatment depleted both macrophages (82 ± 4% depletion) and DCs (46 ± 7% depletion)[56,57].

Mathematical modelling. Assumptions, derivations, as well as parameter values and distributions, obtained by applying Markov Chain Monte Carlo simulations, can be found in Supplementary Section 'Mathematical material'.

Agonistic activity of pMHC–NPs *in vitro*. FACS-sorted splenic $CD8^+$ or $CD4^+$ cells from TCR-transgenic mice (2.5×10^5 cells ml^{-1}) were incubated with a range of pMHC-conjugated or control NP concentrations for 24–48 h at 37 °C. The supernatants were assayed for IFNγ by ELISA.

Responsiveness of human T-cell clones was assessed by culturing 5×10^5 T cells in 48-well plates, in 500 μl of complete RPMI-1640 media containing anti-CD3/anti-CD28 mAb-coated beads (Life Technologies; at a bead-to-cell ratio of 1:1), $PPI_{76-90(88S)}$/DRB1*0401-coated PF-M (50 μg of pMHC/ml) or an identical number of control, Cys-coated PF-M. On day 2, supernatants were collected for cytokine analyses by Luminex and cell pellets harvested for RNA extraction. In other

© 2017 Macmillan Publishers Limited, part of Springer Nature. All rights reserved.

experiments, T-cell clones were incubated with $PPI_{76–90(88S)}$/DRB1*0401-coated PF-M or Cys-coated PF-M for up to 5 days. Cells were collected on days 0, 2, 3, 4 and 5 and used for RNA extraction.

Flow cytometry. 5×10^4 T cells were resuspended in 50 µl of FACS buffer containing 4 µl FcR blocking reagent (Miltenyi Biotec), incubated for 15 min at room temperature and further incubated with anti-CD4-FITC (clone OKT4), anti-CD45RA-V450 (BD Biosciences), anti-CD49b-APC (Biolegend) and anti-LAG-3-PE (R&D) antibodies for 30 min on ice or at 37 °C, respectively. Cells were washed, resuspended in 200 µl FACS buffer and analysed with a FACSCanto II (Becton Dickinson). All stainings were done in the presence of an anti-CD16/CD32 mAb (2.4G2; BD Pharmingen) to block FcRs. Analysis was done using FlowJo software.

Human T-cell clones were stained with FITC-conjugated anti-CD4 (OKT4, BioLegend), APC-conjugated anti-CD19 (HIB19, BD Pharmingen), PerCP-conjugated polyclonal goat anti-LAG-3 IgG (R&D), biotin-conjugated anti-CD49b (AK7, Pierce Antibodies, Thermo Scientific), and EF450-conjugated streptavidin (eBioscience).

TEM. Human T-cell clones, thioglycollate-induced peritoneal macrophages, bone marrow-derived DCs or BDC2.5-$CD4^+$ and 8.3-$CD8^+$ T cells (5×10^6 ml^{-1}) were incubated with $PPI_{76–90(88S)}$/DRB1*0401-coated PF-M, BDC2.5mi/IA^{g7}- and NRP-V7/K^d-coated PF-M NPs for 30 min at 4 °C (15–20 µg ml^{-1} of pMHC). The cultures were further incubated at 37 °C for the indicated lengths of time, washed with cold PBS, fixed and sectioned (70 nm) for TEM imaging with a Hitachi H7650.

Super-resolution microscopy. 8.3-$CD8^+$ T cells were incubated with NRP-V7/K^d-PF-M-Alexa-647 NPs at 4 °C for 30 min or at 37 °C for another hour. Cells were washed three times with cold PBS pH 7.4, then fixed in 2% paraformaldehyde (PFA) for 15 min on ice. After washing, cells were stained with 1 µg ml^{-1} DAPI at room temperature for 5 min, mounted and observed under a super-resolution microscope (ELYRA 131, Zeiss). Image processing and quantitative analysis of cluster diameter was done with ZEN 2012 software ($n = 100$).

SEM and X-ray spectrometry. Cells were plated on a coverslip and incubated with unconjugated or Cys-conjugated PF-M, BDC2.5mi/IA^{g7}-PF-M or NRP-V7/K^d-PF-M at 4 °C for 30 min with/without additional 60 or 180 min incubations at 37 °C. After washing with 0.05 M cacodylate buffer pH 7.4, samples were fixed with 2.5% glutaraldehyde at 4 °C overnight, subjected to sequential dehydration in graded ethanol and immersed in hexamethyldisilazane for 3 min for drying. The samples were observed under an XL30 SEM (Philips) by gold coating. Element analysis was carried out using energy-dispersive X-ray spectrometry (EDS).

Generation of pMHC–PF-M-specific human TR1-poised cell clones. PBMCs, obtained from individuals recruited under informed consent approved by the Institutional Review Board at Hospital Clinic, were isolated from heparinized blood by gradient centrifugation and resuspended at 5×10^6 ml^{-1} in complete RPMI-1640 (Gibco) media supplemented with 10% human AB serum (Linus). The cells were cultured in 24-well plates in the presence of human pre-proInsulin (PPI) 76-90(S88) peptide (SLQPLALEGSLQSRG) at 10 µg ml^{-1}. A stimulation control culture was performed with 2 µl ml^{-1} Pediacel (Sanofi-Pasteur), a penta-vaccine. After 7–10 days, cells were washed, and cultured for 5 days in wells coated, at high density, with avidin and biotinylated $PPI_{76–90(88S)}$/DRB1*0401 monomer. Finally, cells were cultured for 5 additional days in the presence of 1 µg ml^{-1} of soluble anti-hCD28 mAb (BD Pharmingen). A low dose of interleukin-2 (2.5 units ml^{-1}) (R&D) was added on day 2. Presence of antigen-specific T cells in the $CD4^{high}CD25^+$ T-cell subpopulation was evaluated by flow cytometry after staining with PE-labelled $PPI_{76–90(88S)}$/DRB1*0401 tetramer. $Tetramer^+$ $CD4^+$ T cells were single-cell sorted into 96-well plates using a FACSAriaII sorter (Becton Dickinson). Individual cells were expanded into clones for 15 days by stimulation with irradiated PBMCs (10^5 per well) in RPMI-1640 media with 1 µg ml^{-1} phytohemagglutinin-P (PHA-P) (Sigma) and 100 U ml^{-1} of human interleukin-2. On day 15, $tetramer^+$ clones were expanded by re-stimulation with irradiated PBMCs (10^6 per well) in RPMI-1640 media containing PHA-P and interleukin-2.

Cytokine/chemokine secretion by macrophages and DCs. Ten-week-old NOD mice were left untreated or were treated with 10 doses of BDC2.5mi/IA^{g7}-PF-M NPs (20 µg pMHC per dose; 2 doses per week for 5 weeks). Splenic $CD11b^+$ and $CD11c^+$ cells were isolated from collagenase D-digested cell suspensions (2 mg ml^{-1}, Roche Diagnostics) using CD11c microbeads (Militenyi Biotec) or CD11b magnetic particles (BD Biosciences). Cells (10^5) were cultured for 3 days with BDC2.5mi/IA^{g7}-PF-M NPs (20 µg pMHC ml^{-1}) or vehicle alone. The supernatants were analysed using Multiplexing LASER Bead Assay technology (Eve Technologies).

Quantitative RT-PCR. RNA was subjected to QRT-PCR using primers specific for human IL-21 (Forward: CCAAGGTCAAGATCGCCACA; Reverse: GGCAGAAATTCAGGGACCAAG), IL-10 (Forward: AAGACCCAGACATCAAGGCG; Reverse: AATCGATGACAGCGCCGTAG), IFNγ (Forward: CAGGTCATTCAGATGTAGCGGA; Reverse: TCTGTCACTCTCCTCTTTCCAA), c-Maf (Forward: GAGAAGTTGGTGAGCAGCGG; Reverse: GCGAGTGGGCTCAGTTATGAA), LAG-3 (Forward: CCTCACTGTTCTGGGTCTGG; Reverse: CAGCGTACACTGTCAAGGGA), and CD49b (Forward: CGGGCAAATTATACCGGCCA; Reverse: GGAGCCAATCTGGTCACCTC).

Stability of pMHC–NPs in mouse serum. NRP-V7/K^d-NPs were incubated with serum for 0, 1, 2 and 4 h at 37 °C, washed in PBS through 100KD amicon ultrafiltration units and incubated with cognate 8.3-$CD8^+$ T cells (5×10^4 per well) for 48 h at 37 °C (2.2 µg of pMHC per well) in 96 U-bottomed well plates. The IFNγ content in the culture supernatants was measured by ELISA.

Biodistribution of pMHC, unconjugated NPs and pMHC-conjugated NPs. pMHC and pMHC–NPs were labelled with Cyto670-NHS ester in 0.2 M dicarbonate buffer, pH 9.5 for 1.5 h at room temperature, purified by Amicon Ultra15 (30 kDa) and re-suspended in PBS, pH 7.2. Unconjugated NPs were incubated with free cysteine overnight, washed via ultrafiltration (10 kDa) and labelled with cyto670 as above. Cohorts of 8-week-old male NOD mice were injected with fluorochrome-labelled pMHC, -NP or -pMHC–NPs. Blood and the indicated organs were harvested at 1, 4, 8 and 24 h after treatment. Fluorescence intensity of tissue samples was measured using a Carestream Multispectral MS Fx Pro *in vivo* imager under fluorescent excitation of 650 nm and emission wavelength at 750 nm. Images were subject to normalized background subtraction in ImageJ, followed by mean fluorescence intensity measurements for each organ area. The mean fluorescence intensity was subtracted from the organs of control mice given PBS injections. Absolute fluorescence intensity values in different organs were normalized to the total cumulative fluorescence intensity of all organs combined, for each time point analysed.

Half-life measurements. Cohorts of 8-week-old male NOD mice were injected with cyto670-labelled pMHC–NPs or NPs, and tissues collected at 1, 4, 8 and 24 h post-injection. The half-life times in individual tissues were then calculated according to tissue-specific one phase exponential decay curves using Graphpad Prism software.

Zebrafish embryo development toxicity screen. PBS in PF-M or pMHC–PF-M was exchanged to embryo medium (5.0 mM NaCl, 0.17 mM KCl, 0.33 mM CaCl, 0.33 mM $MgSO_4$; $NaHCO_3$ to pH 7.4) prior to making stock solutions for testing. At 4 h post-fertilization, embryo chorions were removed enzymatically and the embryos transferred to individual wells of a 96-well plate with 100 µl of prepared NP solution[58]. Embryos were exposed to 50, 10, 1 µg ml^{-1} of each NP preparation (normalized to Fe content) and to an embryo medium control ($N = 24$ embryos (wells) per treatment, 1 plate per NP type). The static NP exposure was maintained at 28 °C until 24 h post-fertilization (h.p.f.), at which time developmental progress and mortality were assayed. At 120 h.p.f., embryos were assessed for their escape response to a gentle touch with a blunt probe to the head and tail region. They were then euthanized by tricaine overdose and scored for mortality and morphological malformations. For malformation statistics, only embryos that survived were accounted for. Seventeen morphological endpoints were evaluated[59,60].

Serum cytokine 'storm' effect assessment. Pre-diabetic 10-week-old NOD mice were treated with BDC2.5mi/IA^{g7}-NPs (10 µg pMHC), an equivalent amount of unconjugated NPs or human injectable saline as a sham injection control. Serum samples were taken before and 8 h after treatment and used to measure 32 different cytokines and chemokines via Luminex.

Haematology, biochemistry and histological analyses. Cohorts of 8-week-old NOD male mice were treated with 200 µl PBS, pH 7.4, or with a single dose of unconjugated or pMHC-conjugated PF-M containing 200 µg Fe in 200 µl PBS, pH7.4. Mice were sacrificed 1, 3, 10, 30 and 100 days after injection. On intravenous administration, the animals were monitored for signs of complications (for example, weight loss, dehydration, lethargy, and so on). Mice were anaesthetized and blood collected via cardiopuncture into microvette tubes containing lithium/heparin and K3 EDTA for blood biochemistry and haematology, respectively. The urine was collected in concerts of bladder voiding on euthanasia, and puncturing the bladder post-mortem. Haematological analyses were performed by the Centre for Modeling Human Disease (CMHD, Toronto, Canada) within 24 h using a Hemavet 950FS analyser. The biochemistry analyses were done by IDEXX Laboratories using a Beckman Coulter Olympus AU5811 analyser. Urine analysis was performed by dispensing 10 µl per spot of the urine samples on colorimetric Chemstrip 5 OB (Roche). Liver, kidney, spleen, femurs, brain and axillary/bronchial/inguinal lymph nodes were also collected post-mortem on days 10, 30 and 100 after treatment, and processed for haemotoxylin and eosin (H&E) staining and histopathology.

TEM of kidney. Cohorts of 10-week-old mice were injected with pMHC–NPs ($n = 3$; 25 µg of iron per dose, twice a week for 5 weeks) or Ferumoxytol (Faraheme; $n = 3$, also at 25 µg of iron per dose, twice a week for 5 weeks). One day after the last dose, mice were sacrificed and their kidneys sectioned for TEM. A third cohort of mice ($n = 3$) was injected with a single dose of pMHC–NPs (200 µg of iron) and sacrificed 4 h later to collect the kidneys. Images were captured using a Hitachi H7650 TEM.

© 2017 Macmillan Publishers Limited, part of Springer Nature. All rights reserved.

Statistical analyses. Quantitative data were compared by Student's *t*-test (for $n > 30$) or Mann–Whitney U test (for $n < 30$). Qualitative data were compared via Chi-Square test on contigency tables. Pearson correlation was used to establish correlations between two values. Two-way ANOVA tests were used to determine how a response was affected by two variables. Sample sizes were calculated based on available data and the intrinsic experimental variability of the different assays used. Statistical significance was assumed at $P < 0.05$.

Data availability. The data that support the plots within this paper and other findings of the study are available from the corresponding author upon reasonable request.

References

42. Katz, J. D., Wang, B., Haskins, K., Benoist, C. & Mathis, D. Following a diabetogenic T cell from genesis through pathogenesis. *Cell* **74,** 1089–1100 (1993).
43. Verdaguer, J. *et al.* Spontaneous autoimmune diabetes in monoclonal T cell nonobese diabetic mice. *J. Exp. Med.* **186,** 1663–1676 (1997).
44. Han, B. *et al.* Developmental control of $CD8^+$ T cell-avidity maturation in autoimmune diabetes. *J. Clin. Invest.* **115,** 1879–1887 (2005).
45. Garboczi, D. N., Hung, D. T. & Wiley, D. C. HLA-A2-peptide complexes: refolding and crystallization of molecules expressed in *Escherichia coli* and complexed with single antigenic peptides. *Proc. Natl Acad. Sci. USA* **89,** 3429–3433 (1992).
46. Altman, J. D. *et al.* Phenotypic analysis of antigen-specific T lymphocytes. *Science* **274,** 94–96 (1996).
47. Yu, Y. Y., Netuschil, N., Lybarger, L., Connolly, J. M. & Hansen, T. H. Cutting edge: single-chain trimers of MHC class I molecules form stable structures that potently stimulate antigen-specific T cells and B cells. *J. Immunol.* **168,** 3145–3149 (2002).
48. Holst, J. *et al.* Generation of T-cell receptor retrogenic mice. *Nat. Protoc.* **1,** 406–417 (2006).
49. Amrani, A. *et al.* Progression of autoimmune diabetes driven by avidity maturation of a T-cell population. *Nature* **406,** 739–742 (2000).
50. Stratmann, T. *et al.* The I-Ag7 MHC class II molecule linked to murine diabetes is a promiscuous peptide binder. *J. Immunol.* **165,** 3214–3225 (2000).
51. Perrault, S. D., Walkey, C., Jennings, T., Fischer, H. C. & Chan, W. C. Mediating tumor targeting efficiency of nanoparticles through design. *Nano Lett.* **9,** 1909–1915 (2009).
52. Xie, J., Xu, C., Kohler, N., Hou, Y. & Sun, S. Controlled PEGylation of monodisperse Fe_3O_4 nanoparticles for reduced non-specific uptake by macrophage cells. *Adv. Mater.* **19,** 3163–3166 (2007).
53. Xu, C. & Sun, S. Monodisperse magnetic nanoparticles for biomedical applications. *Polym. Int.* **56,** 821–826 (2007).
54. Afonin, K. A. *et al.* Design and self-assembly of siRNA-functionalized RNA nanoparticles for use in automated nanomedicine. *Nat. Protoc.* **6,** 2022–2034 (2011).
55. Li, Y. & Boraschi, D. Endotoxin contamination: a key element in the interpretation of nanosafety studies. *Nanomedicine* **11,** 269–287 (2016).
56. Nikolic, T., Geutskens, S. B., van Rooijen, N., Drexhage, H. A. & Leenen, P. J. Dendritic cells and macrophages are essential for the retention of lymphocytes in (peri)-insulitis of the nonobese diabetic mouse: a phagocyte depletion study. *Lab. Invest.* **85,** 487–501 (2005).
57. Calderon, B., Suri, A. & Unanue, E. R. $CD4^+$ T-cell-induced diabetes, macrophages are the final effector cells that mediate islet β-cell killing: studies from an acute model. *Am. J. Pathol.* **169,** 2137–2147 (2006).
58. Mandrell, D. *et al.* Automated zebrafish chorion removal and single embryo placement: optimizing throughput of zebrafish developmental toxicity screens. *J. Lab. Autom.* **17,** 66–74 (2012).
59. Truong, L., Harper, S. L. & Tanguay, R. L. Evaluation of embryotoxicity using the zebrafish model. *Methods Mol. Biol.* **691,** 271–279 (2011).
60. Truong, L. *et al.* Multidimensional *in vivo* hazard assessment using zebrafish. *Toxicol. Sci.* **137,** 212–233 (2014).

© 2017 Macmillan Publishers Limited, part of Springer Nature. All rights reserved.